A widespread compositionally bimodal tephra sourced from Volcán Melimoyu (44°S, Northern Patagonian Andes): Insights into magmatic reservoir processes and opportunities for regional correlation

C.A. Geoffroy [a, b], B.V. Alloway [c, d, *], À. Amigo [b, e], M.A. Parada [a, b], F. Gutierrez [f], A. Castruccio [a, b], N.J.G. Pearce [g], E. Morgado [b, h], P.I. Moreno [i]

[a] Departamento de Geología, Facultad de Ciencias Físicas y Matemáticas, Universidad de Chile, Santiago, Chile
[b] Centro de Excelencia en Geotermia de Los Andes (CEGA), Facultad de Ciencias Físicas y Matemáticas, Universidad de Chile, Santiago, Chile
[c] School of Environment, The University of Auckland, Private Bag, 92019, Auckland, New Zealand
[d] Centre for Archaeological Science (CAS), School of Earth and Environmental Sciences, University of Wollongong, Wollongong, NSW, 2522, Australia
[e] Servicio Nacional de Geología y Minería (SERNAGEOMIN), Red Nacional de Vigilancia Volcánica, Temuco, Chile
[f] Geoexpeditions, Las Barrancas 25, Pirque, Santiago, 9480000, Chile
[g] Department of Geography & Earth Sciences, Aberystwyth University, Wales, UK
[h] Institute of Geophysics and Tectonics, School of Earth and Environment, University of Leeds, UK
[i] Instituto de Ecología y Biodiversidad, Departamento de Ciencias Ecológicas, Universidad de Chile, Santiago, Chile

ARTICLE INFO

ABSTRACT

We describe the stratigraphy, age, constituent geochemistry and phenocryst thermobarometry of a closely spaced Holocene tephra couplet from Volcán Melimoyu (VMm), located in the Northern Patagonian Andes. The lower tephra unit (La Junta Tephra, Mm-1) is distinctly banded comprising a dominant lower layer of rhyodacitic (~70% SiO_2) pumiceous ash and lapilli (Mm-1p) that abruptly transitions to a subordinate upper scoriaceous layer (Mm-1s) of basaltic andesite composition (~53% SiO_2). This bimodality within Mm-1 contrasts significantly with the closely overlying Santa Ana Tephra (Mm-2) that has a homogeneous trachyte-dacite (~63% SiO_2) composition and is intermediate between the two magmatic end members of Mm-1. We propose a genetic affiliation between Mm-1 and Mm-2, and that the latter event likely represents a hybridised-remnant of those discrete magmas involved in the earlier Mm-1 eruption. To test this hypothesis we applied whole rock elemental mixing and fractional crystallisation model to reproduce the composition and crystallinity of Mm-2. Results indicate that Mm-2 can be reproduced by mixing ~70% Mm-1p with ~30% Mm-1s, with subsequent ~13% fractional crystallisation of plagioclase, and minor amphibole, orthopyroxene, magnetite and biotite.

Equilibrium P-T conditions calculated from Mm-1p phenocrysts point towards magma residency at moderately shallow depths (200—290 MPa, ~7—10-km depth, 850—1000 °C), whereas Mm-1s phenocrysts indicate higher overall P-T conditions (240—480 MPa, ~8.5—17-km depth, 1080—1150 °C). P-T conditions determined for Mm-2 (~290 MPa, ~10-km depth, 930—1000 °C) are similar to those of Mm-1p. There is no physical and/or geochemical evidence of mafic magma involvement in the Mm-2 eruption.

Similar compositionally bimodal tephra are known from other Northern Patagonian Andean centres (i.e. Playas Blanca-Negra Tephra, Antillanca; Lepue Tephra, Michimahuida; Ho and H3 eruptions of Hudson) suggests that the intrusion of mafic magma into more silicic magma bodies is a common occurrence throughout this Andean sector. These widely dispersed, compositionally bimodal tephra not only provide key insights into pre-eruptive magmatic conditions and triggering processes, but can also be readily identified geochemically, and thereby be more fully utilised within future hazard- and paleoenvironmental-related studies.

© 2018 Elsevier Ltd. All rights reserved.

---

* Corresponding author. School of Environment, The University of Auckland, Private Bag, 92019, Auckland, New Zealand.
E-mail address: brent.alloway@gmail.com (B.V. Alloway).

1. Introduction

Compositional zoning of magmas has been noted at many

volcanic centres typically within arc settings worldwide. Initially, the origin of this zoning was controversial (Eichelberger et al., 2000, 2001; de Silva, 2001) with chemical heterogeneities within discrete eruptive events attributed to either: a) zoned reservoirs formed *by in-situ* fractional crystallisation of mafic magma (Smith, 1979; Wolff et al., 1990; Firth et al., 2016) or; b) by the intrusion of mafic magma into a more silicic magma body (*i.e.* Bacon and Druitt, 1988; Kent et al., 2010; Hernando et al., 2016; Singer et al., 2016) and/or inter-connected magma bodies. However, nowadays with the availability and breadth of precise microanalytical (grain-discrete) tools that can be used to characterise magmatic constituents, determining those factors directly influencing the type and tempo of compositional zoning is becoming more common-place. Many centres within the Southern Volcanic Zone (SVZ) of the Andes typically range from mafic cinder cones to volumetrically larger stratovolcanoes with basaltic through to rhyodacitic compositions with potential for sub-kilometer to kilometer-scale lateral partitioning of sub-volcanic magmatic bodies and conduits (*see* Shane et al., 2017). Compositional zoning is well documented within eruptive products from Quizapu (Hildreth and Drake, 1992; Ruprecht et al., 2012) and Hudson Volcanoes (Kratzmann et al., 2009; Weller et al., 2014). Mafic recharge-induced reheating of silicic magma and subsequent magma viscosity reduction leading to enhanced degassing has been implicated to trigger large eruptive events at these centres.

In this study, we analyse two closely spaced tephra layers from Volcán Melimoyu (VMm), a large stratovolcano located in a remote area of southern Chile, that exhibit contrasting characteristics. We first refine the tephrostratigraphic work of Naranjo and Stern (2004) and produce a series of detailed stratigraphic columns showing the correlation of Mm-1 and Mm-2 (equivalent to MEL1 and MEL2, respectively) from key descriptive sections located at medial distances from VMm. Previous volume estimates are re-evaluated. We then conduct geochemistry and thermobarometry of glass and mineral constituents from this tephra couplet to ascertain the temperature and depth of sub-volcanic magma (bodies) beneath VMm, explore possible causative factors involved in their triggering as well as evaluate temporal magmatic relationships between these two closely spaced eruptions. Our ultimate objectives are to better understand magmatic processes in this remote sector of Northern Patagonia, as well as characterise the resultant eruptive products so that they can be effectively utilised as regional chronostratigraphic markers.

1.1. Geological setting

Volcán Melimoyu (44°05′ S, 72°53′W; 2408 m above sea level) is a little studied composite stratovolcano located in a remote area of southern Chile (Stern, 2004; Stern et al., 2007) and within the southern segment of the Southern Volcanic Zone (SVZ) of the Andes (see Fig. 1). VMm is a larger-than-average edifice compared to other SVZ centres (~142 km^3; Völker et al., 2011) constructed of basalt, andesite and dacite lava flows (López-Escobar et al., 1993). The volcanic massif is broadly elongated ~10 km in an E-W direction with a ~1 km diameter summit crater and is permanently ice-covered. The areas surrounding VMm are sparsely populated, with La Junta (~1200 residents) located along the Carretera Austral (Ruta 7) being the largest settlement situated in the area, ~39 km to the northeast and downwind of the volcano.

Most volcanoes within this segment of the SVZ (with the exception of Vn Hudson) are typically located along, or west of, a major structural feature known as the Liquiñe-Ofqui Fault Zone (LOFZ). This zone is marked by a set of north-northeast-trending lineaments, faults and ductile shear zones that parallels the magmatic arc from near the Nazca-South America-Antarctica triple

junction and extends northwards for ~1000 km (Cembrano et al., 2000). Numerous monogenetic mafic cinder cones are similarly roughly aligned along the LOFZ trend indicating a clear structural influence upon the spatial distribution of emergent volcanism with different sources within this region (Gutierrez et al., 2005).

1.2. Evidence of explosive activity centred at Volcán Melimoyu

While there have been no historical accounts of activity, two prominent and closely spaced pumiceous lapilli layers (MEL1 (lower) and MEL2 (upper)) were identified in the pioneering cover-bed reconnaissance work of Naranjo and Stern (2004) close to present-day ground surface in road sections eastwards of VMm. A series of stratigraphic columns and provisional isopachs were constructed for this closely spaced tephra 'couplet' with non-Dense-Rock Equivalent (non-DRE) volumes determined. Radio-carbon ages of ~2.8 and 1.7 ^{14}C ka BP were similarly determined for MEL1 (T-04F and T07, charcoal) and MEL2 (T-04B, bulk 'organic soil'), respectively (Naranjo and Stern, 2004; see Table 1).

The occurrence of Melimoyu-sourced tephra has also been noted within soil-dominated cover-bed and lake sequences within the Río Cisnes valley (44°20′-44°50′S, ~120 km SE from the volcano) (Stern et al., 2015; Weller et al., 2017). For example, Stern et al. (2015) analysed 18 tephra layers within lake cores and glacial-lacustrine sediment outcrops. Based on their petrography and chemistry, six of those layers were ascribed a Melimoyu-source, with two layers in two separate cores correlated with MEL2 (Naranjo and Stern, 2004). Older tephra of presumed Melimoyu-source were identified at 4.6−4.8, 8.3 and 19.7 cal. ka BP (see also tephra layers E, M and O of Weller et al., 2017) but no subaerial exposures of these same tephra have so far been recognised. Further north towards Vanguardia (*this study*, see Fig. 2) and to the south toward Coyhaique, no Melimoyu-sourced tephra have so far been recognised (Weller et al., 2015, 2017).

In this study, informal tephra designations (Mm-1 (lower) and Mm-2 (upper)) are equivalent to MEL1 and MEL2, respectively, as previously assigned by Naranjo and Stern (2004). However, our intention is to formalise Mm-1 and Mm-2 in accordance with the International Stratigraphic Guide (e.g. Murphy and Salvador, 1999) and ascribe new geographical place-names and reference sections (see Supplementary Information 1.0). Consequently, Mm-1 and Mm-2 are renamed La Junta and Santa Ana Tephra, respectively. The rationale for this formalisation is outlined in Alloway et al. (2017b) and intended to remove numeric labelling of eruptive units and/or any inference to eruptive source.

2. Results

2.1. Stratigraphy and age

Two transects (N−S and W-E) are presented to show spatial variability of Mm-1 and Mm-2, as well as the presence of tephra inter-beds originating from other eruptive centres (i.e. Vga-tephra from the Vanguardia Cone Complex (VCC)) (Figs. 2 and 3; Table 1). At all described sections, the lower tephra (Mm-1) is distinctly banded comprising a dominant lower layer of white pumiceous ash and lapilli (Mm-1p) that abruptly transitions to a subordinate upper dark-grey scoriaceous layer (Mm-1s). This banding significantly contrasts with the closely overlying Mm-2 comprised entirely of shower-bedded white pumiceous ash and lapilli. Radiocarbon ages determined from charcoal material immediately underlying Mm-1 and Mm-2 (this study; see Table 1) are indistinguishable from those originally determined for MEL1 and MEL2, and confirm a late Holocene age with eruptions separated by ~1100 years. One aspect of the cover-bed stratigraphy that
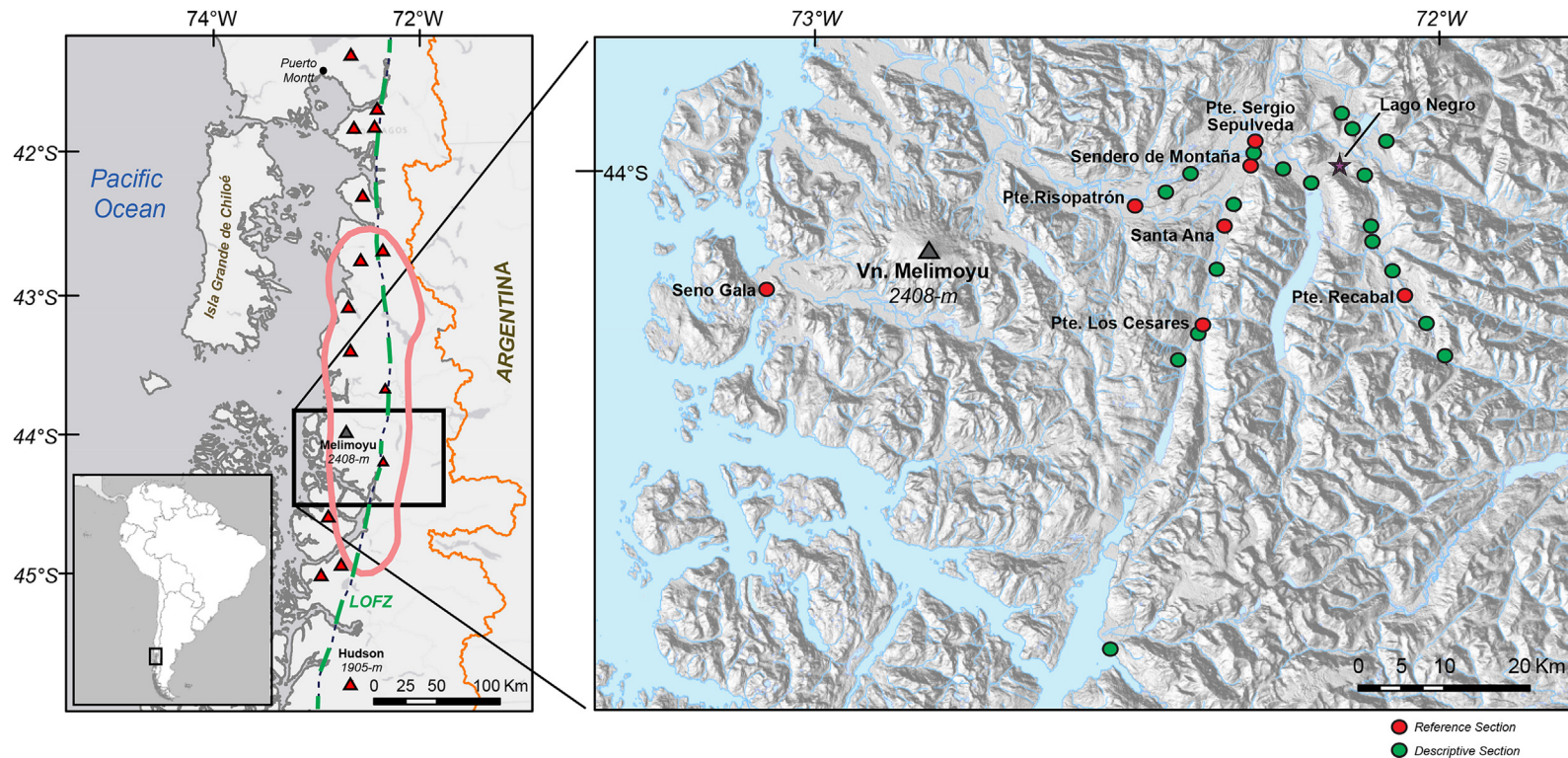
Fig. 1. Map showing the location of volcanoes (red triangles) distributed within the southern portion of the Southern Volcanic Zone (SVZ). Volcán Melimoyu (VMm; 2408-m) is indicated as a grey triangle. Most stratovolcanoes (with the exception of Vn Hudson) and monogenetic basaltic cone complexes are typically located along, or west of, a major N-S trending structural feature known as the Liquiñe-Ofqui Fault Zone (LOFZ; indicated as a dashed green line). The community of La Junta (~1200 residents) is located in the immediate vicinity of the Sendero de Montaña reference section and is located ~39 km to the northeast of VMm. The pink-coloured contour defines an erosion 'hotspot' where modelled erosion rates are >0.6 mm/year (Herman and Brandon, 2015). This region of Patagonia was extensively glaciated during the Last Glacial Maximum (LGM). Consequently, except for ice-sculptured outcrops located on the volcanic edifices themselves, most range-front and valley cover-bed stratigraphies in this region are post-glacial in age. Reference and descriptive sites are indicated and occur in medial distances (<60 km) from eruptive source. Also indicated is the location of Lago Negro (~50 km SE of VMm) where sediment coring has recently been undertaken and is likely to provide a much higher resolution eruptive record sourced from VMm and other SVZ centres that would otherwise be identified from equivalent-aged soil successions within the same region. (For interpretation of the references to colour in this figure legend, the reader is referred to the Web version of this article.)

Table 1
Radiocarbon dates and ages acquired (this study) from late Holocene Melimoyu-sourced tephra (Mm-1 and Mm-2) as well as stratigraphically associated tephra from other eruptive sources (see Fig. 2). Radiocarbon dates obtained for MEL1 (Mm-1) and MEL2 (Mm-2) by Naranjo and Stern (2004) are included for comparison.

Location	Lat./Long.	Lab/Sample ID	Sample type		^{14}C AMS age (^{14}C a BP)	^{14}C Calibrated Age (±2σ) (cal. a BP)	95% HPDF[a] (cal. a BP)
Mm-2							
Seno Gala (MEL115-13)	S 43 42′ 28.4″ W 72 20′ 19.8″	Beta Analytical −425606	Charcoal	Immediately below lower contact	1650 ± 30	1493 ± 84	1416–1568
MEL2 (Naranjo and Stern, 2004)	S 44 09.1′ W 72 28′	T04B	'Organic Soil'	Bulk sample underlying lower contact	1750 ± 80	1607 ± 202	1412–1814
Mm-1							
Pte Los Cesares (MEL115-1)	S 44 08′ 34.0″ W 72 27′ 42.4″	UCIAMS-145940	Charcoal	Immediately below lower contact	2505 ± 20	2559 ± 96	2379–2710
Sendero de Montana	S 43 58′ 26.6″ W 72 24′ 07.9″	UCIAMS-145939	Charcoal	Immediately below lower contact	2715 ± 20	2784 ± 54	2748–2845
MEL1 (Naranjo and Stern, 2004)	S 44 09.1′ W 72 28′	T04F	Charcoal	Closely underlying lower contact	2790 ± 70	2856 ± 158	2738–3005
	S 44 03.6′ W 72 25.8′	T07	Charcoal	Immediately below lower contact	2740 ± 70	2808 ± 160	2702–2991
Vanguardia	S 43 42′ 28.4″ W 72 20′ 19.8″	UCIAMS-145488	Bulk carbonac. mud	Immediately below lower contact	5930 ± 25	6707 ± 74	6643–6785
		UCIAMS-145489	Wood in growth position	Immediately below lower contact	5910 ± 25	6691 ± 80	6568–6780
		UCIAMS-145490	Wood in growth position	Immediately below lower contact	5955 ± 25	6730 ± 84	6660–6829
		UCIAMS-145941	Bulk carbonac. mud	Immediately below lower contact	5905 ± 25	6686 ± 84	6567–6776
		UCIAMS-145942	Wood in growth position	Immediately below lower contact	6015 ± 25	6607 ± 96	6696–6897
	R_combine modelled age ($n = 4$)				5925 ± 13	6703 ± 58	6652–6775

[a] **Highest Probability Density Function**.

is immediately apparent is the paucity of older (mid-to early-Holocene) macroscopically visible tephra beds locally sourced from VMm as well as other adjacent and far-field eruptive centres, especially since older Holocene VMm-tephra have been recognised distally (i.e. 120 km to the SE, Stern et al., 2015; Weller et al., 2017).

2.2. Distribution and volume

Isopach curves for Mm-1 and Mm-2 are presented in Fig. 4 with granulometric parameters for selected sections at different distances from eruptive source presented in SI Table 1. For Mm-1, eruptive parameters were separately calculated for both Mm-1p and Mm-1s since they are distinctively different with each sub-unit able to be easily discerned in the field. In acquiring isopach and isopleth data for Mm-1p, Mm-1s and Mm-2 we measured bed thickness and clast-dimensions at twenty-four, eighteen and seventeen sections, respectively.

Volume data was calculated using exponential one- and two-slope (Fierstein and Nathenson, 1992) and Power Law (Bonadonna and Costa, 2012) techniques. Volume data for Mm-1p and Mm-1s are indistinguishable (1.9–2.0 km³ and 0.5–0.6 km³, respectively) between techniques. However, for Mm-2 there is a large discrepancy (0.9–1.6 km³) between both methods (see Table 2), and may be attributed to the lack data in both proximal and distal regions, or the way these techniques integrate an upwind positioned (westward) Mm-2 data point outlier (Seno Gala). Irrespective of this discrepancy, non-DRE volumes calculated for Mm-1 (~1.9–2.1 km³, Mm-1p; ~0.5–0.6 km³, Mm-1s) and Mm-2 (~0.9–1.6 km³) are about a factor of 2–3 times higher (*cf.* 1.4 km³, MEL1; 0.5 km³, MEL2) than those of Naranjo and Stern (2004). Originally, column heights of 29–41 km for Mm-1p, 28–43 km for Mm-1s and 26–31 km for Mm-2 were calculated as per the G3/5 and 5PM methods (Table 2). However, higher values were discarded

as some isopeths were obtained with too few control points leading to possible height over-estimations. Consequently, plume heights are more conservatively estimated to ~30–35 km for Mm-1p, ~30–35 km for Mm-1s and ~26–30 km for Mm-2. Irrespective of this, both eruptions have calculated explosivity indices (VEI) of ~5.

2.3. Mineralogy and geochemistry

Modal mineralogy (vol. %) and mineral characteristics of Mm-1 and Mm-2 are represented in SI Table 2. Mineral phases range from microlites (<10-μm) to phenocrysts of 2-mm in length and include plagioclase, amphibole, and rare orthopyroxene and Fe–Ti oxides for Mm-1p; plagioclase, olivine, clinopyroxene, with rare Fe–Ti oxides for Mm-1s; plagioclase, amphibole, olivine, clinopyroxene, orthopyroxene, Fe–Ti oxides and biotite for Mm-2. Crystal clots (glomerocrysts) were noted within both Mm-1 and Mm-2, with the former unit having higher phenocryst volume (5.4–7.5%) than the latter (<1.9%) (SI Table 2).

Back scatter electron (BSE) images of selected glass shards from Mm-1 (Mm-1p and Mm-1s) and Mm-2 are presented in Fig. 5. Within the glassy matrix of Mm-1p (Fig. 5-A (MM-1) and 5-B (MM-6)) low microlite concentrations are observed along with well-formed oriented vesicles. At the transition between Mm-1p and Mm-1s (MM-7), the microlite concentration within glassy grains increases and vesicles become more irregularly shaped (Fig. 5-C and -D). Banded (mingled) pumices similarly occur within this transition with two distinctly different textural types in direct contact with each other (Fig. 5-E and insets). Higher within the sequence, equant-shaped shards of Mm-1s are characterised by "intensely microlitic glass" where vesicles have completely collapsed and formed coalesced voids (Fig. 5-F and -G). Shards of Mm-2 resemble those of Mm-1p containing sparse microlites but are typically thinner walled and more intensely vesiculated (Fig. 5-
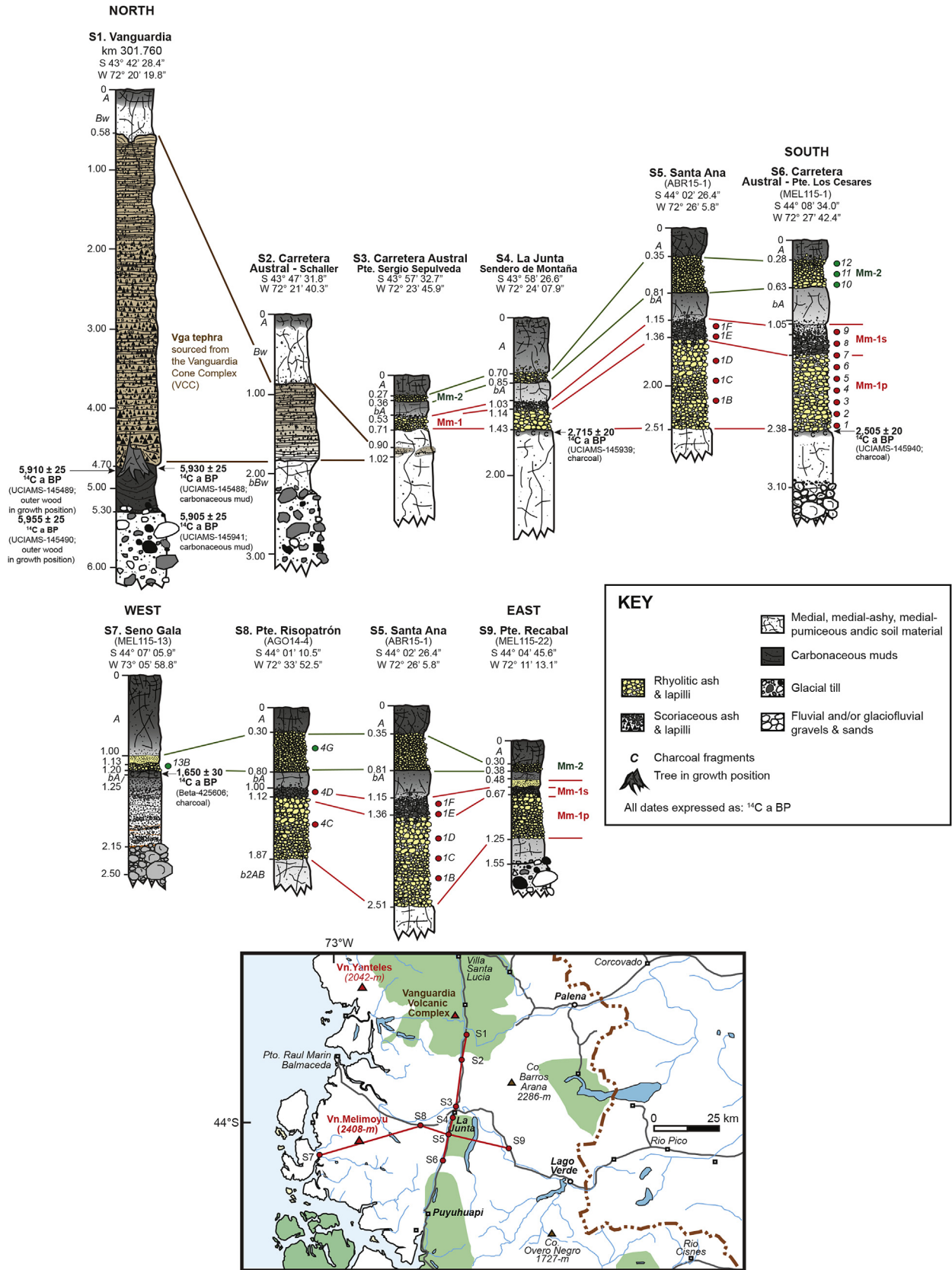
Fig. 2. Stratigraphic columns showing the correlation of the closely spaced tephra couplet (Mm-1 and Mm-2) from key descriptive sections located at medial distances from VMm. Two transects (N-S and W-E) are indicated to show spatial variability as well as the presence of tephra inter-beds originating from other eruptive centres (i.e. Vga-tephra from the Vanguardia Cone Complex (VCC) located ~62 km NE of VMm). The position of radiocarbon dates and geochemical samples are indicated. The inset map shows the distribution of these descriptive sites with respect to VMm.

Fig. 3. The stratigraphies exposed at Pte. Los Cesares (**A, B**), La Junta (**C, D**), Pte. Risopatrón (**E**), Santa Ana (**F**) and Pte. Recabal (**G**) showing the VMm-sourced tephra couplet interbedded with andic soil material and associated dateable charcoal (yellow arrow; see Table 1). At Pte. Sergio Sepulveda (**H**) located *c.* 1.7 km north of La Junta the VMm-tephra couplet is underlain (<30 cm) by a prominent basaltic tephra (Vga) that can be traced northwards along the Carretera Austral (i.e. Schaller section, see **I**) to its eruptive source at the Vanguardia Cone Complex (VCC). Near Vanguardia (see Fig. 2) an array of radiocarbon dates retrieved from outer-tree trunk material in position of growth and enclosing carbonaceous mud immediately underlying a 4.2 m thickness of basaltic fall provide a R-combined modelled age (*n* = 4) of 5925 ± 13 ^{14}C a BP (6703 ± 58 cal. a BP) for this eruptive event (see Table 1). (For interpretation of the references to colour in this figure legend, the reader is referred to the Web version of this article.)
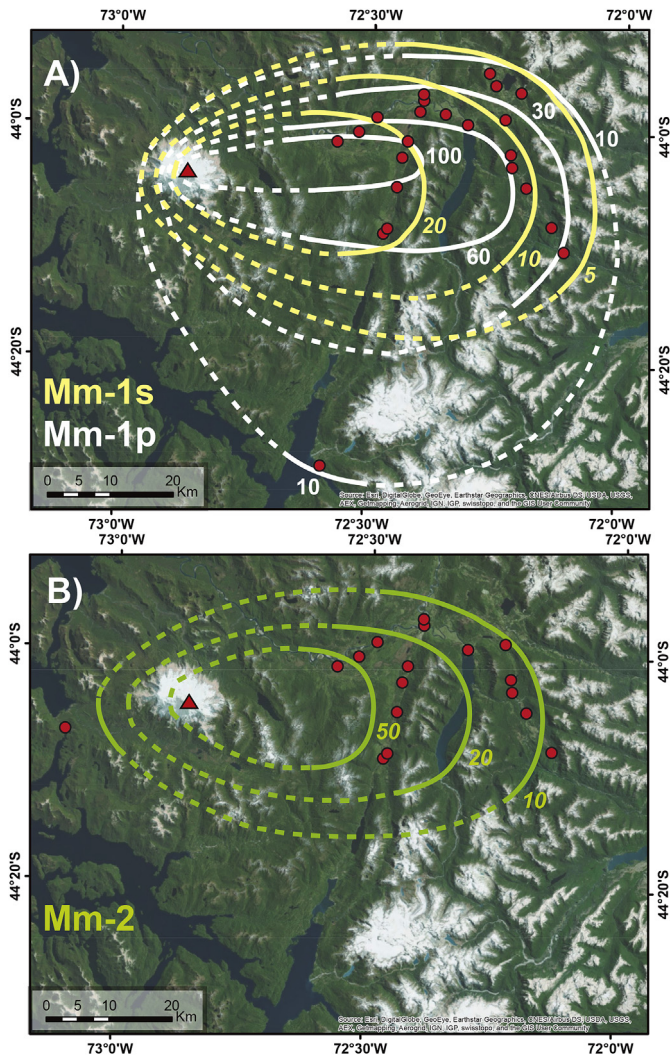
Fig. 4. Isopach Maps for **(A)** Mm-1p (white), Mm-1s (yellow) and **(B)** Mm-2 (green) with thicknesses in centimetres. Please note the paucity of reliable primary thickness data in southern proximal and medial sectors, as well as possible distortion of the Mm-1p 10-cm isopach based on a single southernmost data-point. This isopach demarcated as a dashed line and the estimate of Mm-1p volume derived from it, is therefore regarded as provisional. Point thickness data is available upon request. Granulometric parameters for selected tephra sections at different distances from eruptive source are presented in SI Table 1. (For interpretation of the references to colour in this figure legend, the reader is referred to the Web version of this article.)

H and -I).

Analysing the intensely microlitic glass either by EMPA and/or LA-ICP-MS is highly problematic in that microlites are inevitably included in the material analysed even when using a 20-10 μm diameter EMPA, or LA-ICP-MS, spot (for Methods see

Supplementary Information 2.0). However, with sufficient analyses, glass chemistry can be determined as an end-member to a trend of analyses contaminated by (dominantly) plagioclase phenocrysts, and in some cases "microlite-free" analyses can be produced, particularly so from the microlite-poor glass shards (see Alloway et al., 2017a).

Glass shard major- and trace-element data is presented in SI Tables 3 and 4, while major element mineral data is present in SI Table 5. Major element glass shard elemental data acquired by grain discrete spot and 10 μm EMP analyses (Fig. 6) indicate that Mm-1 has a significant compositional range from rhyolite (Mm-1p; MM-1 to −6) through to trachyte-dacite (e.g. MM-7) to basaltic trachyandesite-basaltic andesite (Mm-1s; samples MM-8 and MM-9) (utilising the classification scheme of Le Maitre, 1984). For Mm-1p (MM-1 to −6), the major element composition is tightly clustered but transitioning into Mm-1s above (i.e. MM-7), compositions dramatically shift becoming more mafic. Common banded (mingled) pumices are observed within this transitional zone. For Mm-1s (MM-8 and -9) spot and 10 μm analyses of interstitial glass were conducted (Fig. 6 and SI Table 3), in an effort to reduce the excitation of crystal contaminants and optimize glass data. Aside from slight variance in alkali elemental concentrations as a result of increased beam-induced volatilization during spot analysis, all other elemental concentrations remain very similar, and verify that the interstitial glass matrix of Mm-1s is of intermediate composition ($\sim$53–54% SiO_2). Glass shard elemental data for Mm-2 indicates a tightly clustered borderline trachyte-dacite ($\sim$63% SiO_2) composition (Fig. 7), which is intermediate between, and on the same trend as, the two magmatic end members of Mm-1. Mm-2 glass shard major elemental data indicate a subtle upward change in composition through the tephra deposit (Fig. 7) that appears to reflect magma chamber zonation.

Selected trace element (Zr, Th, Sr, Nb) compositions of glass shards from Mm-1 as determined by grain discrete LA-ICP-MS analyses are presented in Fig. 8. All data display a range of compositions ranging from pure rhyodacitic glass with a tight compositional cluster averaging $\sim$161 ppm Sr (i.e. microlite-free analyses from microlite-poor glass shards; i.e. MM-1 to −6) to high-Sr compositions ($\sim$470 ppm Sr) where the glasses become increasingly microlite-rich, with higher Sr compositions coming from analyses which have ablated feldspar, with very little glass in the intensely microlitic shards (i.e. MM-8 and-9). With increasing Sr, incompatible element concentrations decrease, associated with low incompatible element concentrations in feldspar. All analyses were calculated using the glass SiO_2 composition from the shards (determined by EPMA) as the internal standard (I.S.). This will give accurate analyses for the pure glass component (i.e. low Sr analyses), but the change in glass composition by inclusion of feldspar in the analyses will mean that, as more feldspar is ablated, the true SiO_2 content of the ablated mixture (the I.S. composition) moves further from the pure glass composition and the analyses will become progressively less accurate (see Pearce, 2014; Alloway et al.,

Table 2
Calculated eruptive parameters for late Holocene explosive eruptions from Volcán Melimoyu.

Unit/Eruption	Volume[a] (km³)	Volume[b] (km³)	Volume[c] (km³)	Column height (km) G3/5	Column height (km) 5PM	Dispersal direction
Mm-2	0.9	1	1.6	26–31	27–31	E
Mm-1s	0.6	0.5	0.5	28–43	30–43	E
Mm-1p	2.1	1.9	1.9	29–41	30–41	E-SE

References.
[a] Exponential one slope (Fierstein and Nathenson, 1992).
[b] Exponential two slope (Fierstein and Nathenson, 1992).
[c] Power Law (Bonadonna and Costa, 2012).

Table 3

Whole-rock major- and trace-element compositions determined by (A) XRF and (B) ICP-MS techniques. Mm-1p and Mm-1s layers of Mm-1 collectively correspond with MEL1 (Naranjo and Stern, 2004). Similarly, Mm-2 corresponds with MEL2.

Sample	SiO$_2$	TiO$_2$	Al$_2$O$_3$	FeO*	MnO	MgO	CaO	Na$_2$O	K$_2$O	P$_2$O$_5$	Total	LOI	Ni	Cr	Sc	V	Ba	Rb	Sr	Zr	Y	Nb	Ga	Cu	Zn	Pb	La	Ce	Th	Nd	U
XRF	Major and minor elements (oxides wt. %)												Unnormalised trace elements (ppm)																		
Mm-2																															
MEL115-13B	59.22	1.17	16.93	6.23	0.17	1.5	3.91	5.12	2.56	0.40	97.21	2.38	4	4	19	49	614	75	346	367	48	22	21	13	100	15	45	87	11	45	2
AGO14-4G	58.04	1.00	17.73	5.50	0.17	1.56	3.73	5.16	1.92	0.38	95.20	4.22	3	3	14	47	517	51	371	289	39	17	19	6	88	13	33	69	10	35	1
ABR15-5A	56.12	1.11	18.57	5.98	0.17	1.54	3.73	4.93	1.80	0.42	94.37	4.97	3	2	15	54	495	49	375	297	41	17	21	8	92	13	33	74	8	36	2
ABR15-5C	58.67	0.93	17.94	5.40	0.16	1.42	3.64	5.20	2.01	0.35	95.72	3.95	3	1	13	45	535	55	358	302	40	16	21	6	89	13	32	70	9	34	2
Mm-1s																															
AGO14-4D	47.93	1.45	18.62	9.93	0.17	5.08	8.42	3.25	0.71	0.35	95.90	2.90	25	45	33	250	236	16	497	125	24	8	19	57	79	6	17	37	3	20	1
ABR15-1E	48.19	1.46	19.0	9.81	0.17	4.53	7.92	3.39	0.77	0.35	95.60	3.34	21	37	32	249	255	19	488	144	24	9	21	56	82	5	19	41	4	20	1
ABR15-1F	47.14	1.48	19.4	10.11	0.16	4.94	8.27	3.17	0.67	0.34	95.68	3.90	25	44	33	255	225	16	500	132	22	7	20	56	80	6	10	40	4	20	1
Mm-1p																															
AGO14-4C	62.13	0.68	17.01	3.62	0.18	1.00	2.34	5.59	2.24	0.24	95.02	4.21	3	3	6	27	593	57	287	309	34	18	21	3	86	13	33	69	8	33	1
ABR15-1C	62.49	0.68	17.29	3.71	0.17	0.99	2.45	5.62	2.22	0.22	95.85	3.84	3	2	7	25	596	57	300	313	33	18	20	3	87	13	31	70	9	34	2
ABR15-1B	61.91	0.69	17.58	3.73	0.17	1.02	2.55	5.58	2.16	0.23	95.62	3.86	2	3	6	29	592	56	316	311	32	18	20	4	87	14	36	66	8	30	1
ABR15-1D	60.86	0.70	17.83	3.81	0.17	1.04	2.57	5.42	2.09	0.23	94.72	4.75	3	2	8	36	573	54	318	311	33	17	20	3	87	14	31	76	8	32	2

| Sample	La	Ce	Pr	Nd	Sm	Eu	Gd	Tb	Dy	Ho	Er	Tm	Yb	Lu	Ba	Th	Nb	Y	Hf	Ta	U	Pb	Rb	Cs	Sr	Sc	Zr
ICP-MS	Trace elements (ppm)																										
Mm-2																											
MEL115-13B	42	90	11	45	9.8	2.5	9.2	1.5	9.0	1.9	5.1	0.8	4.8	0.8	619	11.2	20.6	47.5	8.7	1.4	2.6	15.3	73.1	3.2	346	18	368
AGO14-4G	34	76	9	37	8.3	2.1	7.7	1.3	7.6	1.5	4.4	0.6	4.1	0.7	527	8.9	15.6	39.8	6.9	1.1	2.0	13.2	51.8	2.3	379	13	294
ABR15-5A	33	75	9	38	8.6	2.3	7.9	1.3	7.9	1.6	4.5	0.7	4.2	0.7	492	8.2	16.0	40.6	7.1	1.1	2.0	13.2	47.2	2.1	373	14	300
ABR15-5C	32	70	9	35	7.7	2.0	7.1	1.2	7.3	1.5	4.1	0.6	4.0	0.6	529	8.3	15.7	38.3	7.2	1.0	2.1	13.4	53.4	2.4	357	12	304
Mm-1s																											
AGO14-4D	16	35	5	20	5.1	1.7	5.0	0.8	4.8	1.0	2.7	0.4	2.3	0.4	231	2.8	7.2	23.9	3.2	0.5	0.7	5.6	16.2	0.6	507	32	129
ABR15-1E	16	42	5	22	5.3	1.7	5.1	0.8	5.0	1.0	2.6	0.4	2.4	0.4	243	3.2	8.0	23.9	3.5	0.5	0.8	6.4	17.2	0.7	486	31	145
ABR15-1F	14	35	4	19	4.7	1.6	4.8	0.8	4.7	0.9	2.4	0.3	2.1	0.3	215	2.9	7.2	21.9	3.2	0.5	0.7	5.7	14.6	0.6	493	32	131
Mm-1p																											
AGO14-4C	35	72	9	34	6.9	1.8	6.1	1.0	6.1	1.3	3.7	0.6	3.7	0.6	613	8.2	17.4	33.6	7.4	1.2	2.0	13.6	57.1	2.3	290	6	316
ABR15-1C	34	71	9	33	6.8	1.8	5.9	1.0	6.1	1.2	3.5	0.6	3.6	0.6	598	8.1	17.1	32.1	7.2	1.2	1.9	13.3	54.9	2.3	296	6	311
ABR15-1B	33	69	8	32	6.7	1.8	5.8	1.0	5.9	1.2	3.5	0.5	3.6	0.6	591	8.1	16.9	31.9	7.1	1.2	1.9	13.1	53.4	2.2	314	6	309
ABR15-1D	32	69	8	31	6.6	1.7	5.8	1.0	5.9	1.2	3.5	0.5	3.5	0.6	573	8.2	17.1	31.5	7.2	1.2	1.9	13.4	51.2	2.1	315	7	311
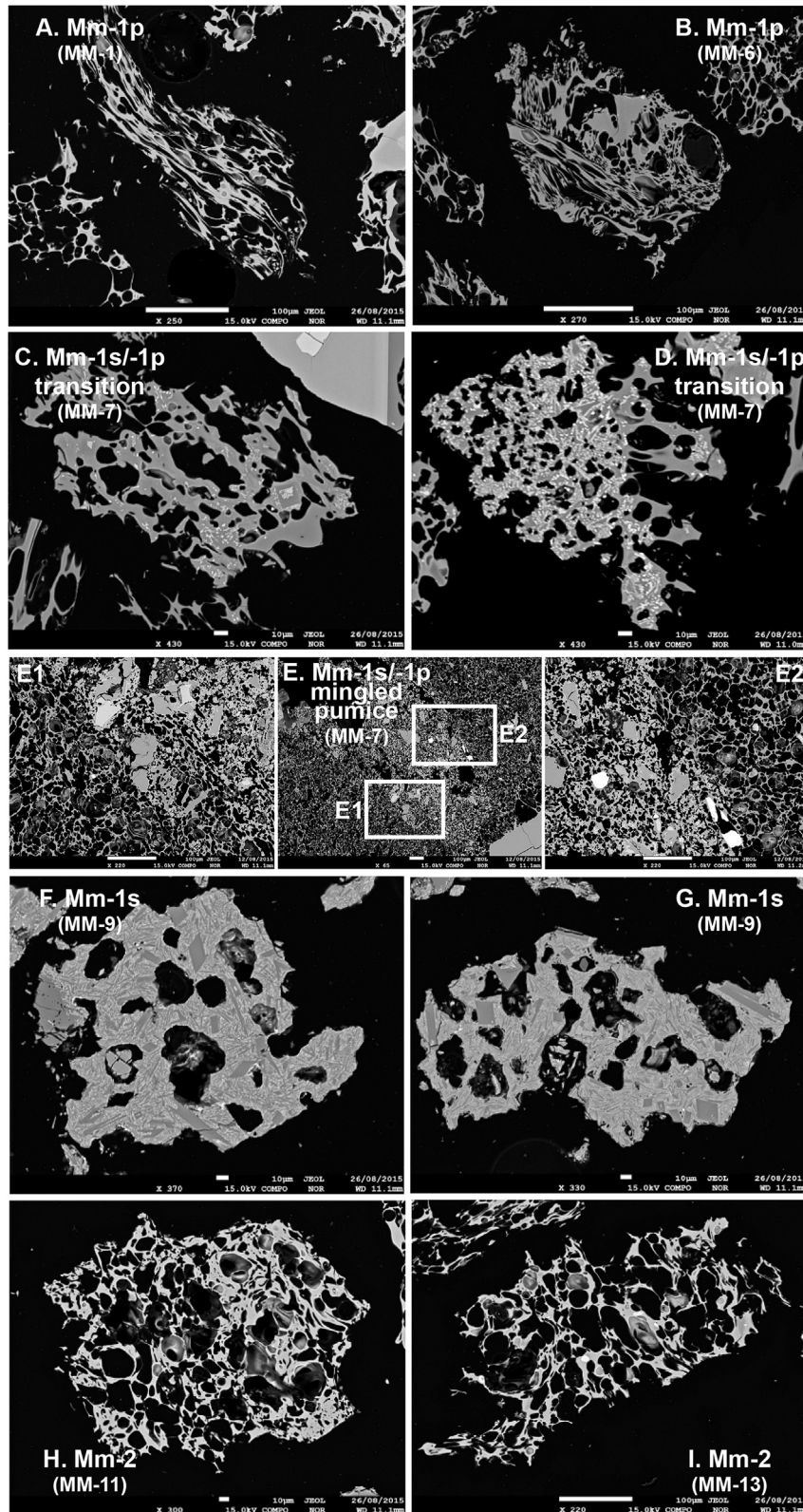
Fig. 5. Selected back-scatter electron (BSE) images of glass shards from Mm-1p, Mm-1s and Mm-2. Low microlite concentrations were observed within glassy grains within Mm-1p (**A, B**), however, at the transition between Mm-1p and -1s (MM-7; see Fig. 2) there is a significant increase in the concentration of microlites within the glassy matrix (**C, D**). E and insets **E1 and E2** indicate mingling of different magmatic constituents within a single pumice occurring at the transition (MM-7) between Mm-1p and Mm-1s. Note that as the microlite concentration increases, the proportion of well-formed oriented vesicles decrease with a corresponding increase in irregular shaped (collapsed) and coalesced voids (i.e. **F, G**). For Mm-1s, the overwhelming dominance of glass grains containing profuse microlites made it very difficult and in many cases, impossible for 10–20 μm diameter electron and laser beams to be positioned on glass and without any obvious microlite contamination. We also conducted spot EMP analyses in order to more accurately characterise the glassy component and reduce possible analytical contamination from microlites. This data is indicated in Fig. 6 and SI Table 2. Images retrieved from upper and lower Mm-2 (**H, I**) indicate a dominantly glassy matrix with well-developed vesicles and few dispersed microlites and sparse mineral phenocrysts.
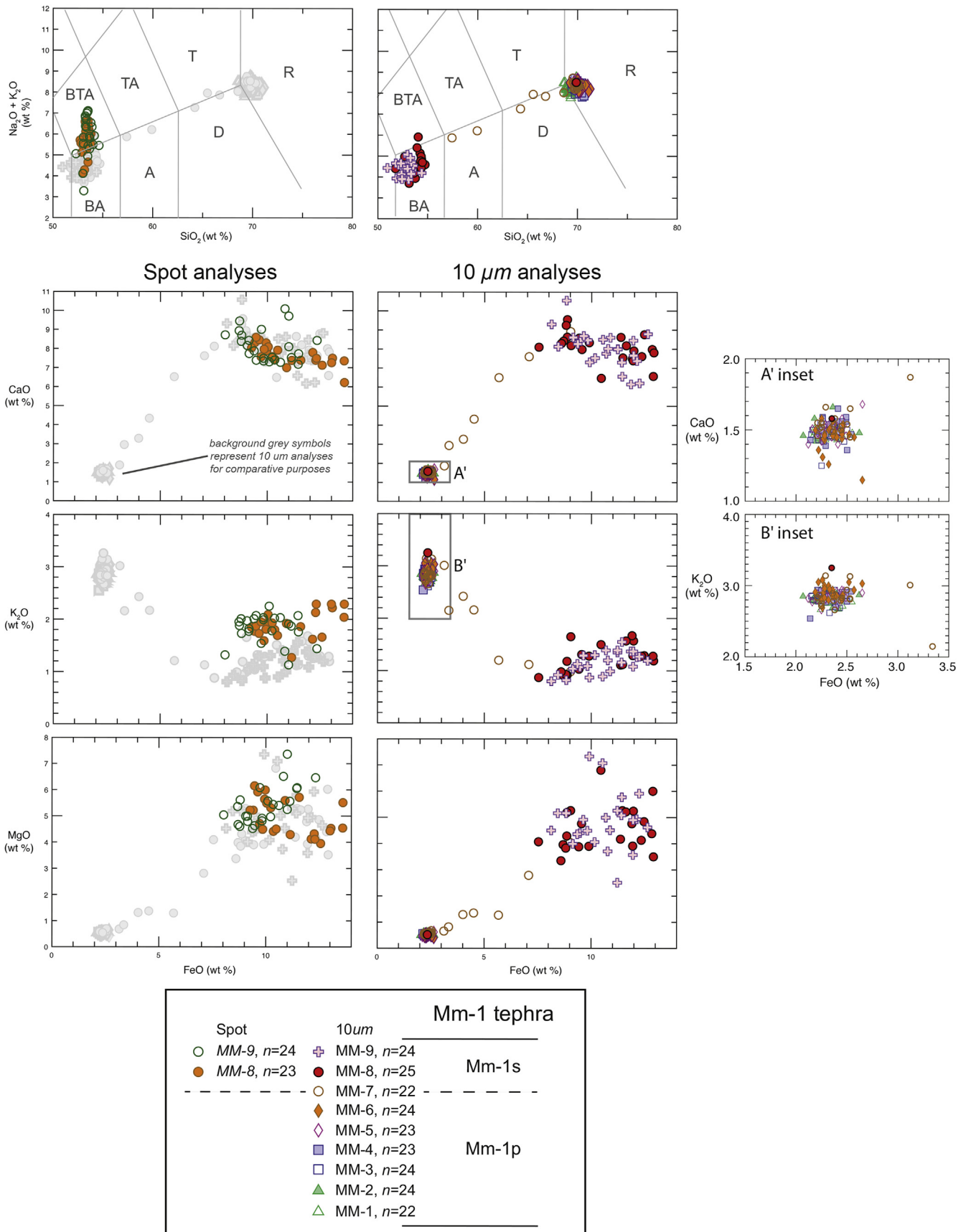
Fig. 6. Selected major element compositions (weight percent SiO$_2$ vs Na$_2$O + K$_2$O and FeO vs CaO, K$_2$O, MgO) of glass shards from Mm-1 tephra exposed at the Los Cesares section (see SI Table 2). For Mm-1, two glass end members - microlite-poor (Mm-1p) and intensely microlitic (Mm-1s), are plotted to show compositional and elemental concentration differences. For samples MM-8 and -9 constituting Mm-1s spot and 10 μm analyses of glassy matrix were conducted, then compared. Aside from slight variance in alkali element concentration as a result of increased volatilization occurring during spot analysis, the remaining major elements remain very similar and verify glassy matrices of intermediate composition (~53−54% SiO$_2$).
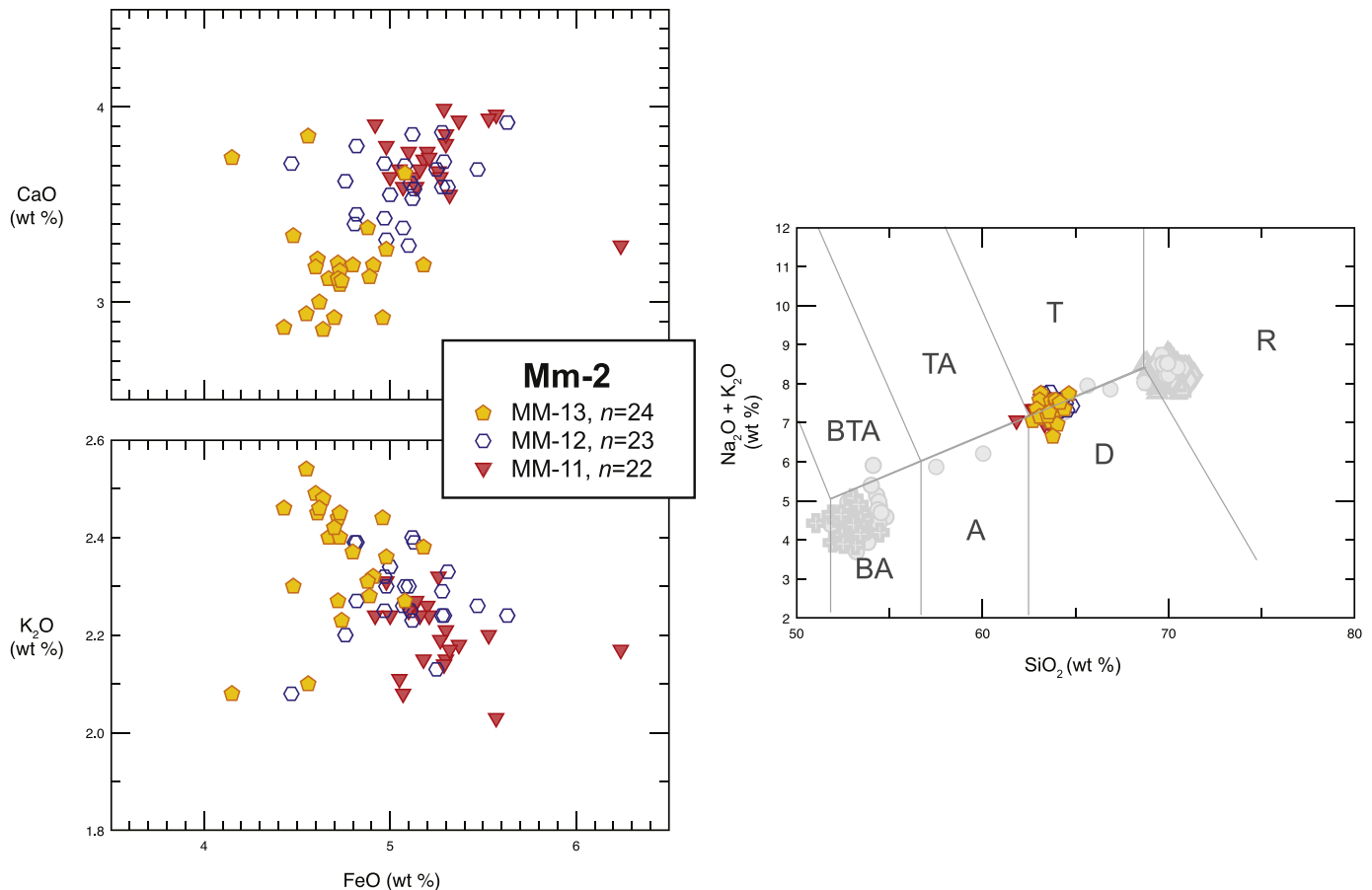
Fig. 7. Selected major element compositions (weight percent SiO_2 vs $Na_2O + K_2O$ and FeO vs CaO and K_2O) of glass shards from Mm-2 tephra exposed at the Los Cesares section (see SI Table 2). Mm-2 tephra has a homogeneous trachyte-dacite (~63% SiO_2) composition and is intermediate between, and on the same trend as, the two magmatic end members of Mm-1 (indicated in grey scale). Note the subtle upward change in composition through Mm-2 appears to reflect magma chamber zonation.

2017b). Incorporation of plagioclase in rhyolitic glass causes the SiO_2 content in the ablated mixture to drop, and thus, using the glass SiO_2 composition as I.S., analysed elements will be marginally overestimated. It is not possible to correct the internal standard concentration for this effect unless the amount of feldspar ablated with glass and the SiO_2 composition of feldspar and glass are both accurately known. The competing effects of dilution of the signal by incorporated feldspar, and changes in reported concentration of determined elements because of changes in the I.S. concentration are discussed in detail in Pearce (2014).

2.4. Phenocryst thermobarometry

In order to determine the temperature and depth of sub-volcanic magma (bodies) beneath VMm, we utilise barometers and thermometers based on mineral geochemistry (see Fig. 9 and SI Tables 3, 4 and 5). Pressure is co-dependant on temperature and vice versa, so P-T values had to be constrained by iterations between geobarometers and geothermometers but also the hygrometer of Lange et al. (2009), by considering different mineral H_2O contents. Fig. 10A shows P-T conditions obtained for the three units utilising amphiboles (Amp) for Mm-1p and Mm-2, and clinopyroxenes (Cpx) for Mm-1s. A summary of temperatures with errors is shown on Fig. 10B.

2.4.1. Mm-1p
The orthopyroxene (Opx)-liquid geothermometer (equation 28a

in Putirka, 2008) and the amphibole (Amp) geothermometer (Ridolfi et al., 2010) techniques were used. The amphibole (Amp)-plagioclase (Pl) geothermometer technique of Holland and Blundy (1994) was also used for Amp-Pl pairs in contact. One orthopyroxene (Opx) rim satisfied the equilibrium conditions with Fe/Mg values of 0.22, whereas four other analyses had Fe/Mg values of ~0.19. Temperatures of ~930−1010 ± 39 °C were calculated from five Opx rims. For Amp core-rim analyses, calculated temperatures were indistinguishable at ~950 °C (core, 916−1006 ± 22 °C; rim, 915−983 ± 22 °C). For paired Amp-Pl, a temperature of ~882 °C (850−902 ± 40 °C) was obtained. Pressure was calculated from the Amp core-rim geobarometer technique of Ridolfi et al. (2010). Pressures of 200−290 MPa were determined (core, 200−424 MPa ± 11%; rim, 187−293 MPa ± 11%).

2.4.2. Mm-1s
The olivine (Ol)−liquid geothermometer (equation 22 in Putirka, 2008) and clinopyroxene (Cpx) geothermometer (Putirka et al., 2003) were used for M1s. The olivine Ol-Cpx geothermometer (Loucks, 1996) was calculated from the only pair that was identified. The equilibrium mineral-liquid conditions were tested using Fe/Mg values (Putirka, 2008). Eleven Ol rims and one core satisfied equilibrium conditions with Fe/Mg values of 0.26−0.29. Ol temperatures of ~1080−1150 °C ± 43 °C were calculated. For Cpx, indistinguishable temperatures of ~1118−1133 °C ± 33 °C and ~1117−1132 °C ± 33 °C were obtained for cores and rims, respectively. By using Ol-Cpx paired rim
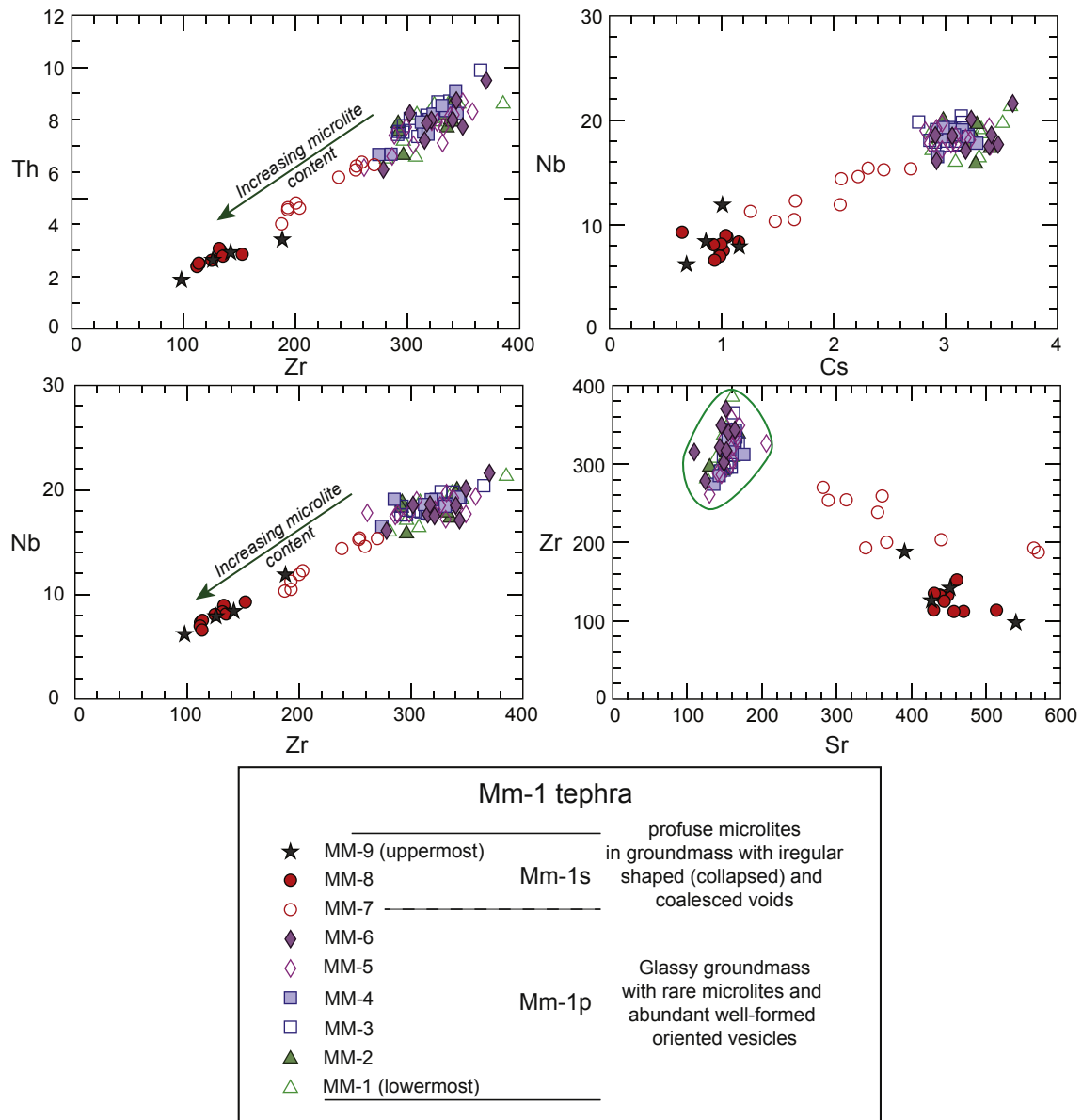
Fig. 8. Zr *vs* Nb and Th, Sr *vs* Zr and Cs *vs* Nb composition of glass shards sampled sequentially through Mm-1 tephra at Los Cesares Section as determined by LA-ICP-MS analysis (see SI Table 3). Microlite-poor (Mm-1p) and intensely microlitic (Mm-1s) glass data are plotted and show significant concentration differences between these two glass types associated with the ablation of (dominantly) plagioclase with glass. The microlite-poor glass compositions typically occur between ~100 and 230 p.p.m. Sr, and these analyses are indicated on the plot of Sr *vs* Zr. See text for explanation.

analyses, a similar temperature of 1100 °C ± 6 °C was obtained. Pressures were obtained from Cpx analyses utilising equation 32a of Putirka (2008), and considering calculated temperatures from Putirka et al. (2003). Pressures between 240 and 480 MPa ± 310 MPa were obtained from both Cpx cores and rims.

2.4.3. Mm-2

The orthopyroxene (Opx)-liquid geothermometer (equation 28a in Putirka, 2008) and the amphibole (Amp) geothermometer (Ridolfi et al., 2010) were used. Two Opx cores satisfied the equilibrium conditions with Fe/Mg values of 0.34–0.35, with an Opx (core) temperature of ~920–980 ± 39 °C determined. With Amp, temperatures of around 970 ± 22 °C (core) and around 990 ± 22 °C (rim) were calculated. Pressures of ~275 MPa ± 11% and 305 MPa ± 11% were also calculated from amphiboles cores and rims, respectively Ridolfi et al. (2010).

2.5. Mixing model

Major-element glass shard compositions (Figs. 6 and 7) indicate that the geochemical heterogeneity within Mm-1 contrasts significantly with Mm-2 which has a homogeneous trachyte-dacite (~63% SiO$_2$) composition between the two compositional end-members of the lower (Mm-1) tephra. In order to explain this compositional difference between two closely spaced eruptions sourced from the same eruptive centre, we have attempted to model the two compositional end-members of Mm-1 against the composition of Mm-2 to ascertain if they are genetically related (see Supplementary Information 3.0 and associated SI Figures). Our mixing model is based on calculations from whole rock major and trace element analyses acquired by Thermo ARL-XRF and ICP-MS (see Supplementary Information 2.0 and SI Table 5). This data suggests that the Mm-2-type composition can be derived by
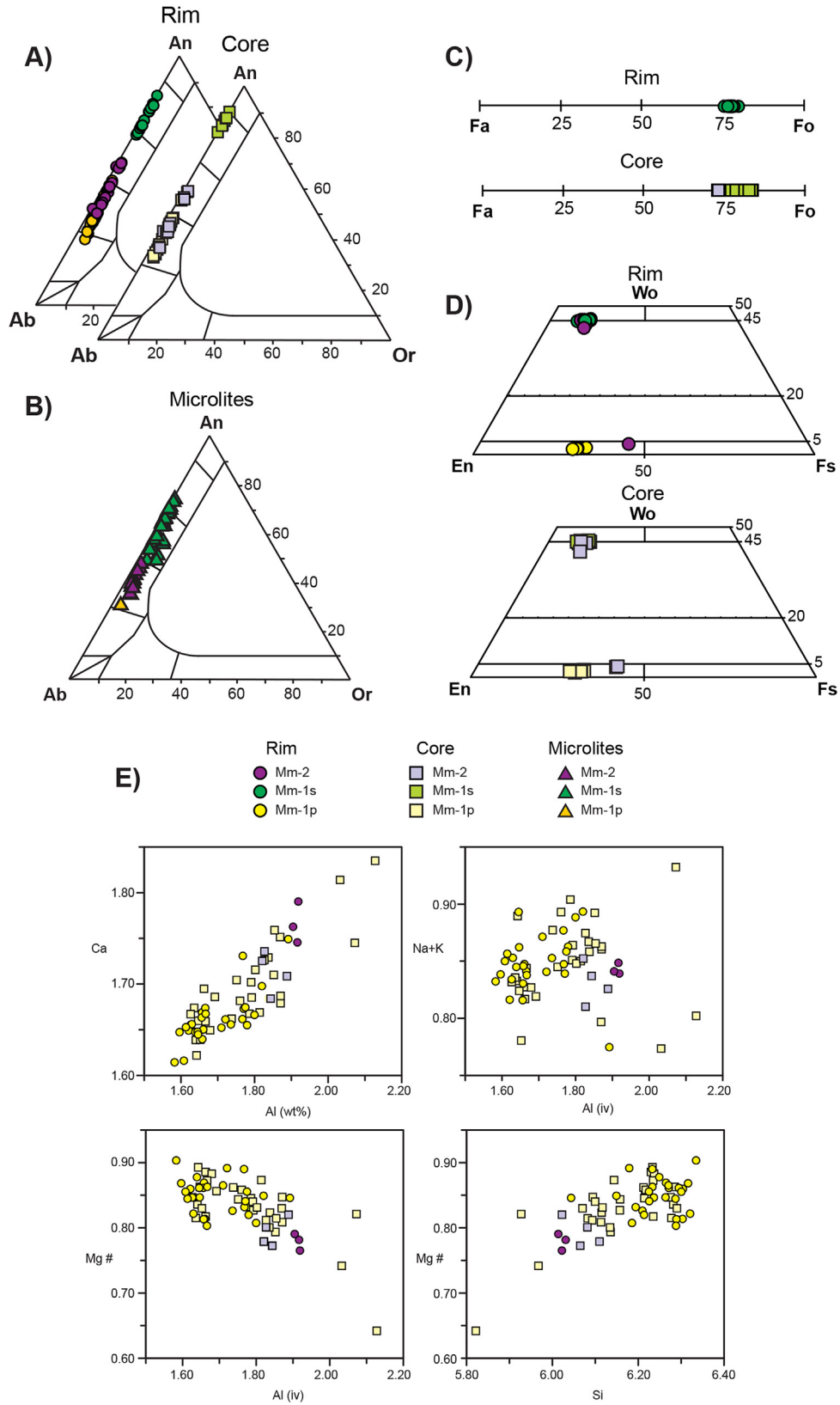
Fig. 9. Rim-core plagioclase phenocryst (A), plagioclase microlite (B), olivine (C) pyroxene (D) and amphibole (E) phenocryst compositions for Mm-1p, Mm-1s and Mm-2 (see SI Table 4).
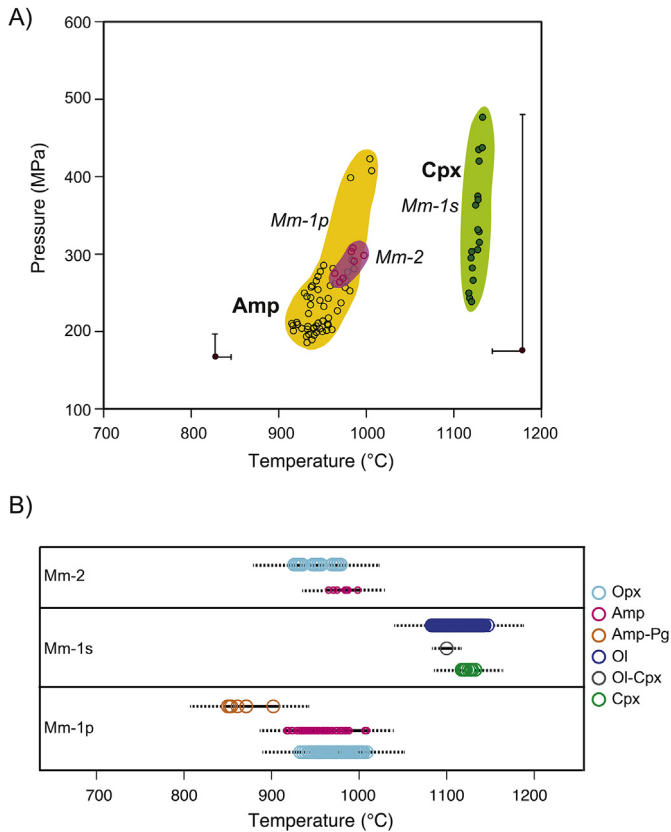
Fig. 10. Phenocryst thermobarometry results for Mm-1 and Mm-2 (see SI Table 4 for phenocryst chemistry). **(A)** Stability P-T fields for amphiboles in Mm-1p (yellow field) and Mm-2 (magenta field) (from Ridolfi et al., 2010) and clinopyroxenes in Mm-1s (green field) (from Putirka et al., 2003; Putirka, 2008). Error bars are indicated; **(B)** Temperatures obtained from amphiboles (after Ridolfi et al., 2010), orthopyroxene (after Putirka, 2008), clinopyroxenes (after Putirka et al., 2003), olivines (after Putirka, 2008), olivine-clinopyroxene (after Loucks, 1996); amphibole-plagioclase (Holland and Blundy, 1994). Dashed lines indicate standard technique errors. (For interpretation of the references to colour in this figure legend, the reader is referred to the Web version of this article.)

mixing from the two end members of Mm-1 in the proportions 63−81% of Mm-1p and 19−37% Mm-1s. However, this outcome was at odds with selected trace-element values (i.e. Rb, La, Ce, Nd, Yb) which are lower (~5−25%) than those values determined for Mm-2 (see Fig. 11). On this basis, we then attempted to reconcile this difference by utilising the Rayleigh equation applied to crystal fractionation.

In the model, trace elements that satisfy the following conditions were used: high ppm concentrations, low analytical errors and wide coefficient distribution reference data. Trace elements chosen were La, Ce, Nd, Eu, Yb, Ba, Nb, Rb, Sr and Zr (see SI Table 6). We also considered phenocryst mineralogy within Mm-2 (i.e. Amp, Opx, Fe−Ti oxides and Bt). Elemental compositions could be described with models of 22−27% crystallisation of plagioclase (50−55%), amphiboles (35−40%) ± othopyroxenes (2−6%), magnetites (3−8%), biotite (~2%).

Application of this equation suggests that in addition to direct mixing (hybridisation) of the two compositional end-members of Mm-1 a further fractionation is required to form a Mm-2-type composition. Model to Mm-2 compositional evolution was achieved by ~24% crystallisation of 49% Pl, 44% Amp, 5% Opx and 2% Bt (see Fig. 12) in the intervening ~1100 years between climactic Mm-1 and Mm-2 eruptions. We corroborate the effect fractional crystallisation on major elements by using a mass balance to obtain the

magma composition of the mixing before crystal fractionation (see Supplementary Information 3.0). Results indicate that mixing about ~70% of Mm-1p and ~30% of Mm1-s before the fractional crystallisation are consistent of both, trace and major elements. The differences between data and the modelled compositions are lower than 5% for trace elements and lower than 1 wt% for major elements.

3. Discussion

3.1. Magma residency based on P-T conditions

A cartoon depicting the conditions and processes involved in the eruption of Mm-1 and Mm-2 is shown Fig. 13. Equilibrium P-T conditions calculated from Mm-1p phenocrysts (Amp, Opx, Amp-Pl) indicate a broad range of values from 187 to 424 MPa and 850−1000 °C and points towards magma residency at moderately shallow sub-volcanic depths (~250 MPa, ~8.5 km depth). Whereas Mm-1s phenocrysts (Ol, Cpx and Ol-Cpx) indicate higher P-T conditions (240−480 MPa, 1080−1150 °C) consistent with residency of this basaltic magma (Mm-1s) at deeper depths and beneath the rhyodacitic magma body (Mm-1) above. Within Mm-1p, pressure conditions of Amp crystallisation decrease with temperature (see Fig. 10A) and can be interpreted as a decompression feature resulting from an ascending plume within the reservoir that interacts with progressively cooler magmas during its ascent. Higher temperatures obtained from Mm-1s implicates this magma body as the thermal source that could activate this Mm-1p plume ascent and trigger the subsequent eruption, which results in the compositionally inverted deposition of reservoir products along with clear evidence of magma mingling at the transition.

3.2. The relationship between Mm-1 and Mm-2

For Mm-2 eruption, there is no clear evidence indicating that intrusion of mafic magma may have been responsible for triggered this eruption (cf. Mm-1), and consequently, its more difficult to recognize the triggering mechanism of this eruption. Analyses of amphiboles (Ridolfi et al., 2010) indicate H_2O contents between 4.6 and 5.0 wt %. By applying empirical solubility laws (Parfitt and Wilson, 2008), the amount of H_2O that can be dissolved in rhyolitic magma at around 250 MPa is calculated at ~5.8 wt% for rhyolite and ~4.5 wt % for basalt. Considering that this eruption has an 'intermediate' composition, the H_2O contents of Mm-2 amphiboles indicate that they crystallised close to water saturation, suggesting volatile oversaturation as a possible eruptive trigger for this Mm-2 event. Such a scenario could be achieved by small amounts of (anhydrous?) phenocryst crystallisation (i.e. Tait et al., 1989).

An alternative possibility to trigger the eruption associated to Mm-2 is a rapid destabilization of a crystalline mush caused by mobilization of volatiles (Bachmann and Bergantz, 2006; Cashman and Sparks, 2014; Cashman et al., 2017; Sparks and Cashman, 2017). According to these authors, melt segregation from a crystalline mush can take place in time scales of 10^3-10^5 years and this can explain the low phenocryst content of Mm-2 compared to both Mm-1p and Mm-1s (SI Table 2). Then, amalgamation and remobilization of fluids can destabilize the magma system in time scales of months to a few years, mobilizing melt-rich accumulations and triggering an eruption. Thus, we consider the hybrid Mm-2 as an interstitial melt extracted and upwardly transported from a crystalline mush formed at the bottom of the reservoir. If heating took place (see Amp T°) then the crystalline mush remobilization and subsequent upward migration of H_2O-rich interstitial melt could occur. This is consistent with decreasing P-T conditions of Mm-2 amphibole crystallisation (see Fig. 10A). The isolated occurrence
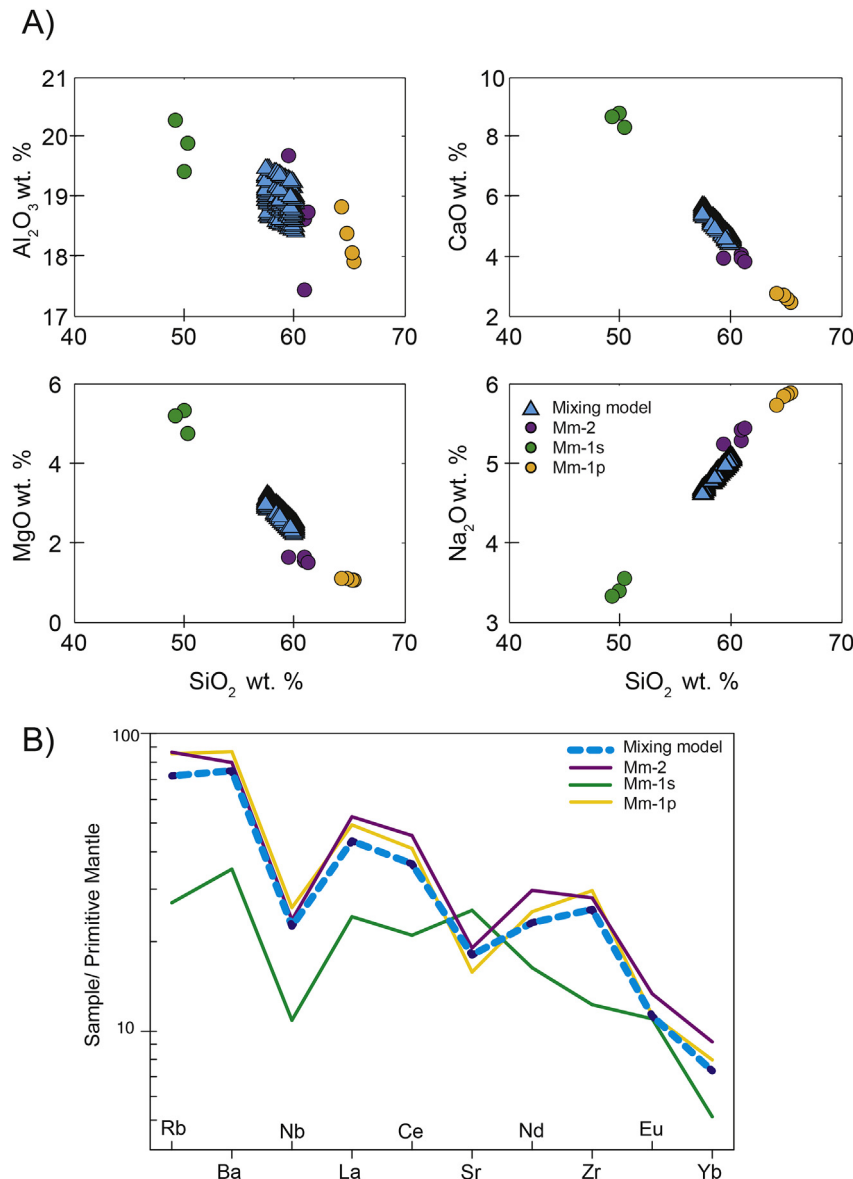
Fig. 11. **(A)** Selected whole-rock major-element mixing models between the two compositional end members of Mm-1 to derive a Mm-2-type mixed composition. Mm-1p, Mm-1s and Mm-2 data-points are represented as coloured circles, while triangle symbols represent the best mixing outcome comprised ~70% of Mm-1p and ~30% Mm-1s; **(B)** Primitive mantle-normalised spider diagram (Sun and McDonough, 1989) and REE patterns (Nakamura, 1974) determined from whole-rock trace-element analyses.

of Cpx-Ol and Opx-Pl crystal clots (glomerocrysts) within this Mm-2 interstitial melt (SI Table 2) lends support to this scenario.

3.3. Paucity of Melimoyu-sourced tephra in the soil-forming environment

Volcán Melimoyu is a volumetrically large stratovolcano (~142 km³) with substantial portions of the edifice permanently concealed beneath ice fields. Its eruptive history is poorly known. In soil-forming successions directly adjacent to VMm only two late Holocene tephra layers are observed (see Fig. 2). However, older distal tephra of Melimoyu-source have been identified in the Río Cisnes valley ~120 km SE (Stern et al., 2015; Weller et al., 2017) but these same tephra have yet to be observed in successions closer to source.

For many years throughout northwestern Patagonia a large number of high-resolution and radiocarbon dateable sediment

cores have been retrieved from bogs and shallow lakes in order to elucidate vegetation-climate change, fire regime shifts and volcanic disturbance (i.e. Moreno and León, 2003; Jara and Moreno, 2012; Pesce and Moreno, 2014; Henríquez et al., 2015). Until recently, the description and characterisation of tephra inter-beds has been a subordinate focus in these dominantly paleoecological investigations. Nowadays, tephra is not only recognised as an essential tool for synchronizing vegetation and climate proxies within equivalent-aged lake records of diverse elevation and latitude (Alloway et al., 2017a), but also highly useful for assessing the tempo of eruptive activity from adjacent and far-field volcanic sources (Moreno et al., 2015; Fontijn et al., 2014, 2016; Weller et al., 2015, 2017). Recently, a ~8.5-m long sediment core was retrieved from Lago Negro (43°58′ 21″S, 72°16′ 20″W) located ~50 km northeast of VMm (see Fig. 1) (PI Moreno, *unpublished data*). At least 78 dm (dm) to millimeter (mm)-thick tephra beds (including Mm-1 and Mm-2) are preserved extending back to 12.9 cal. ka BP during
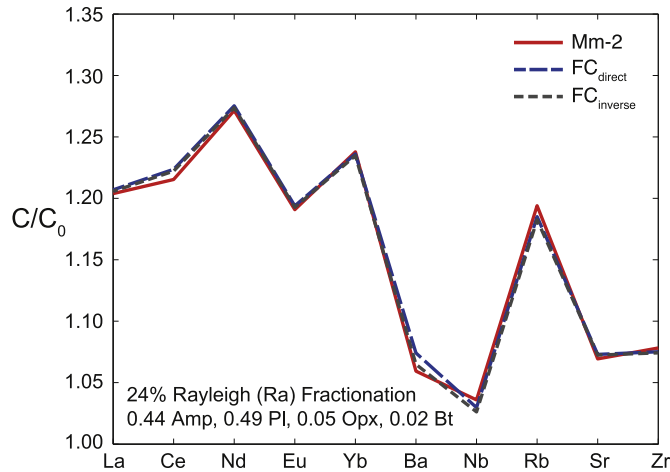
Fig. 12. Rayleigh fractional crystallisation model outcomes (C/C$_o$; Mm-2 mixed model/Mm-2 actual) based on whole rock trace elements (see Table 3).

tephra preserved macroscopically in the soil-forming environment? One possible explanation is heightened precipitation-induced erosion and dispersion of tephra within the soil-forming environment.

Enhanced erosion of tephra appears to be supported by a modelled erosion hotspot centred on the mid-latitude Patagonian Andes (~44°S) (see Fig. 1) that corresponds with both the location of maximum precipitation and erosion rates exceeding 0.6 mm/year (Herman and Brandon, 2015). This erosion hotspot, in the same general vicinity as VMm, is intimately linked to latitudinal shifts in southern westerly winds (SWW) during glacial periods. While changes in strength, position and seasonal evolution of the SWW is becoming better known from modelling and proxy data (Rojas et al., 2009; Rojas and Moreno, 2011; Moreno et al., 2018), it is clear that it exhibits a significant control on coupled atmospheric-ocean circulation changes (Kilian and Lamy, 2012) and plays a fundamental role in determining the distribution and intensity of precipitation and temperature at any given location (Douglass et al., 2005), though the magnitude and rate of erosion may locally vary according to tectonic activity and micro-climate conditions. Therefore the retrieval of high-resolution sediment records like that from Lago Negro will likely provide better opportunities to accurately reconstruct the explosive eruptive history
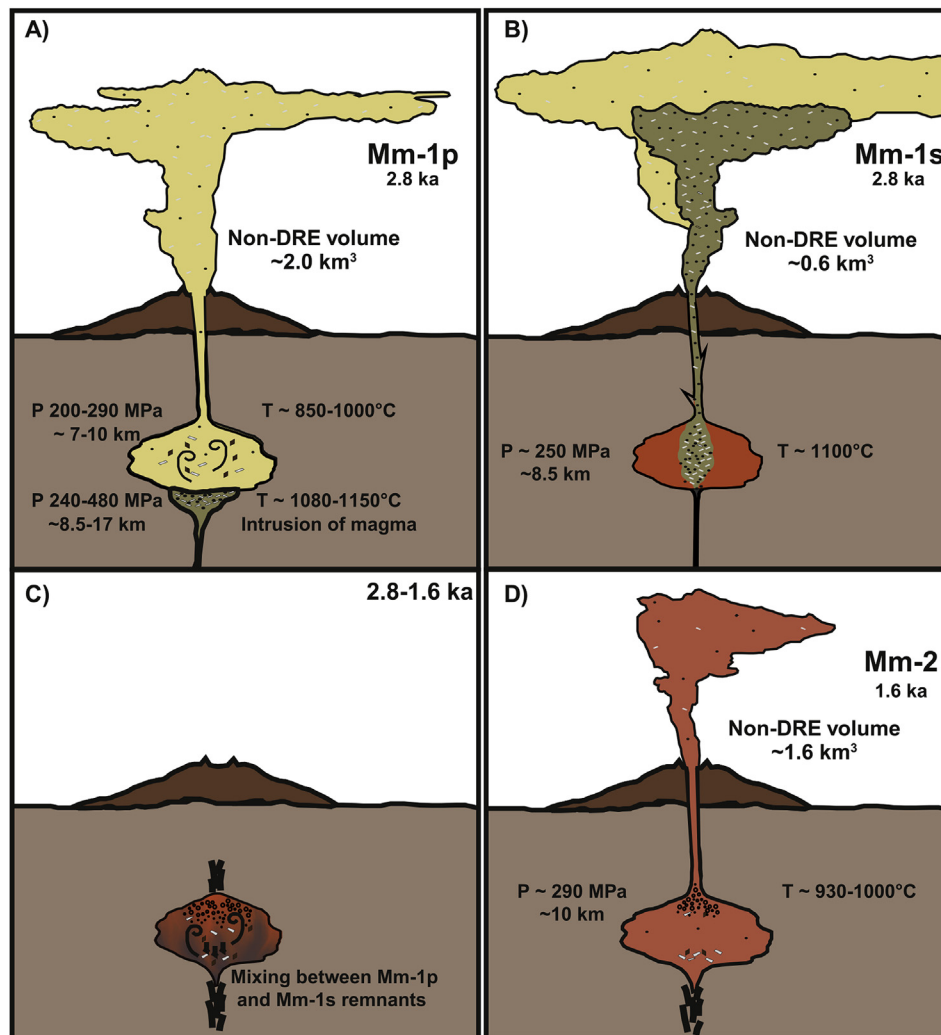
the Last Glacial-Interglacial Transition (LGIT). The obvious question to be raised is why aren't at least some of these more prominent

Fig. 13. Schematic model for Mm-1 and Mm-2 eruptions centred at Volcán Melimoyu. Sub-volcanic equilibrium P-T conditions determined from phenocryst thermobarometry are indicated.
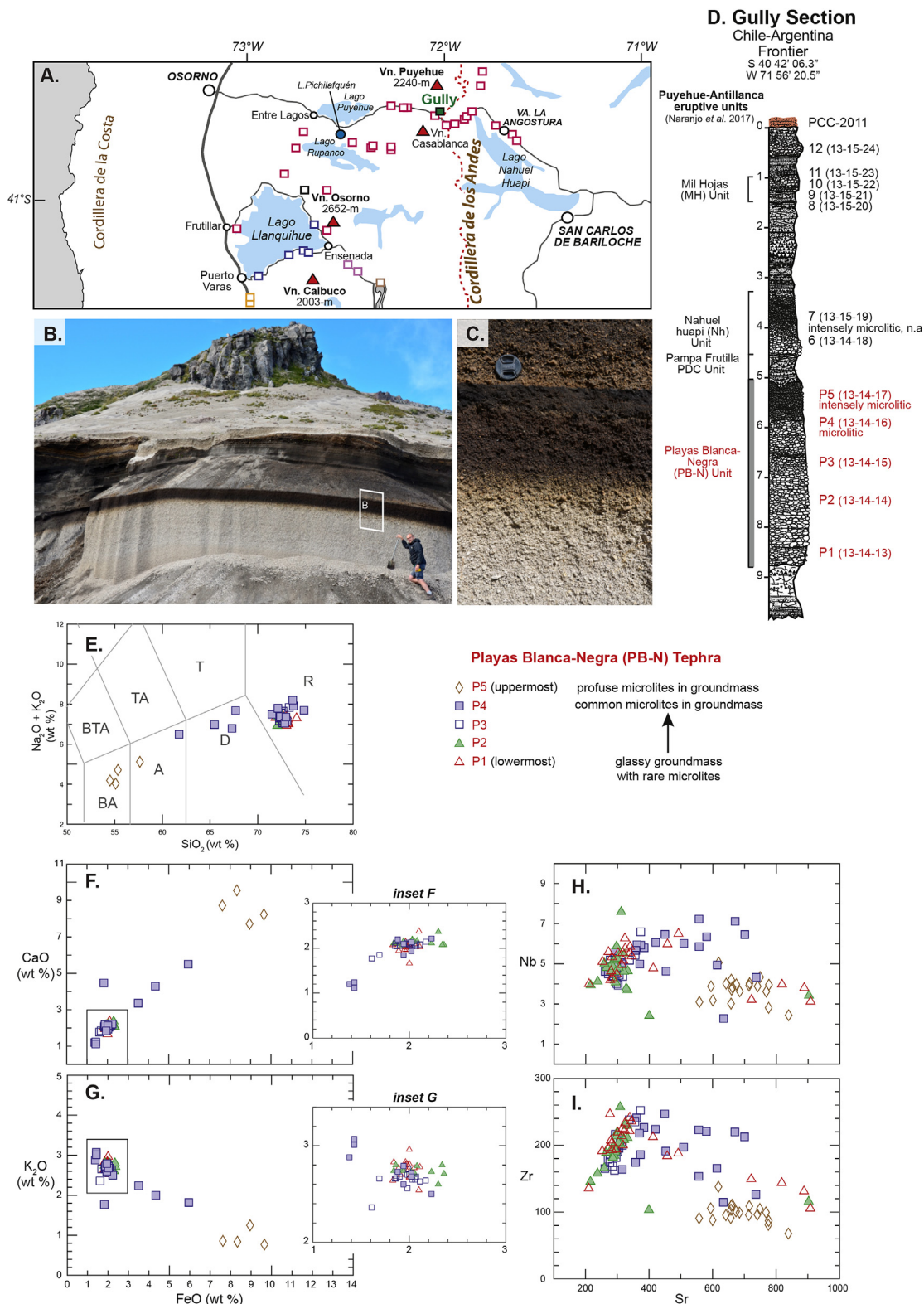
Fig. 14. The stratigraphy associated with Playas Blanca-Negra Tephra sourced from Antillanca caldera (Naranjo et al., 2017) in the vicinity of Paso Cardenal Antonio Samoré on the Chilean/Argentine frontier. The location of the gully section on the inset map is indicated as a green square (**A**). Other coloured squares represent regional survey descriptive sites. The field appearance of this tephra (**B–D**) is strikingly similar to that of Mm-1 with a dominant lower layer of rhyolitic (~74% SiO_2) pumiceous ash and lapilli that abruptly transitions to a subordinate upper scoriaceous layer of basaltic andesite composition (~55% SiO_2). Selected major- and trace-element bivariate glass shard compositions (weight percent SiO_2 *vs* $Na_2O + K_2O$ (**E**); FeO *vs* CaO, K_2O (**F, G**) and Sr *vs* Nb, Zr (**H, I**)) are plotted and show the same upward compositional trends as Mm-1. These trends implicate two compositionally different magma bodies resident within the sub-volcanic system coming into contact, triggering the eruption and resulting in depositional inversion of reservoir products creating a distinctly banded tephra. Other tephra deposits exposed adjacent other volcanic centres in this region exhibit similar field and geochemical characteristics (i.e. Lepue Tephra sourced from Volcán Michmahuida; see Alloway et al., 2017b). (For interpretation of the references to colour in this figure legend, the reader is referred to the Web version of this article.)

of VMm, at least back to the LGIT (12.9 cal. ka BP), than would otherwise be found in equivalent-aged soil-successions.

3.4. Occurrence of similar compositionally bimodal deposits elsewhere within the SVZ

Similar compositionally bimodal (banded) tephra are known from other centres of the northern segment of the Patagonian Andes. For instance, large explosive eruptions sourced from Volcán Hudson, the southernmost volcano of the SVZ (~46°S) have generated several bimodal tephra of late-glacial to Holocene-age (i.e. Ho tephra of Weller et al., 2014). The most recent Hudson eruption (H3 in August 1991) provides a clear example where two compositionally discrete magmas (basalt and trachyandesite with an intervening compositional gap from 54 to 60 wt% SiO_2) were involved and furthermore, were genetically related through both magma mixing and fractional crystallisation (Kratzmann et al., 2009).

Northward of VMm, the c. 11 cal. ka Lepue Tephra erupted from Volcán Michimahuida (~42–43°S) (Alloway et al., 2017a) exhibit similar glass-shard major- and trace-element trends as La Junta Tephra but its magmatic evolution and eruptive history is harder to decipher on account of its antiquity and highly weathered state within soil cover-bed successions. Further northwards (~40–41°S), mingled pumices have been observed within Holocene tephra layers sourced from Volcán Osorno, and the c. 2.2 cal. ka Playas Blanca-Negra (PB–N) Tephra from Antillanca caldera (Singer et al., 2008; Fontijn et al., 2016; Naranjo et al., 2017) spectacularly exhibits a dominant lower layer of rhyolitic (~74 wt% SiO_2) pumiceous ash and lapilli that abruptly transitions to a subordinate upper scoriaceous basaltic-andesite layer (~55 wt% SiO_2) (Fig. 14). Again, major- and trace-element trends for PB-N tephra resemble those indicated for La Junta Tephra (Mm-1) with differences in elemental concentrations reflecting in the former instance, residency of a more silicic magma body (cf. Mm-1) being intersected by mafic magma.

The occurrence of compositionally bimodal tephra throughout this southern Andean sector, suggest that the intrusion of mafic magma into more silicic magma bodies, and sequential involvement of both magmas in the resulting eruption, appears to be a common phenomenon.

4. Conclusion

Holocene activity centred at VMm, deciphered from the soil-forming environment, appears dominated by the two closely spaced explosive eruptions (Mm-1 and Mm-2). Our results show that these eruptions formed plinian eruptive columns of dominantly pumice and scoria juveniles as well as lava lithic clasts forming distinct macroscopic tephra layers up to ~60 km in an east to southeast direction. Based on granulometric parameters, La Junta tephra (Mm-1) has a non-DRE volume of ~2.6 km^3 with an estimated column height of ~30–35 km. Whereas, Santa Ana tephra (Mm-2) has a lesser non-DRE volume of ~1.6 km^3 with an estimated column height of ~25–30 km. Both eruptions have a VEI of ~5.

La Junta (Mm-1) and Santa Ana (Mm-2) tephras have different chemical compositions that show evidence of first, spatial segregation with fringe mingling of two compositionally distinct magmas immediately prior to the first eruption (Mm-1) and second, mixing of Mm-1 magma residues (Mm-1p and Mm-1s) over an interval of ~1100 years to form a hybrid Mm-2 magma. La Junta Tephra is distinctly banded comprising a predominant pumiceous rhyodacitic layer (Mm-1p; ~70% SiO_2) whereas, the upper subordinate scoriaceous layer (Mm-1s) is a basaltic trachyandesite-basaltic andesite (~53% SiO_2). The younger Santa Ana Tephra

(Mm-2) is a trachyte-dacite (~63% SiO_2) and can be modelled by mixing of ~70% of Mm-1p and ~30% of Mm-1s followed by ~13% fractional crystallisation. We suggest that ongoing fractional crystallisation with volatile saturation (secondary-boiling) and/or destabilization (heating by a Mm-1s-type magma) of an underlying crystalline mush causing the upward mobilization of volatile-rich interstitial melts are two potential scenarios involved in the triggering of the explosive Mm-2 eruption (Santa Ana Tephra).

The production of widely dispersed, bimodal and compositionally layered tephra provide clear opportunities for detailed analysis of pre-to syn-eruptive magmatic conditions and triggering processes that serve as useful analogues for volumetrically larger silicic systems being studied elsewhere in the Andes (e.g. Laguna del Maule; Singer et al., 2014, Andersen et al., 2017). Our study reaffirms that these bimodal eruptive products provide excellent stratigraphic markers, that can be readily identified, characterised and widely correlated, and hence have considerable potential to be integrated within future hazard- and paleoenvironmental-related studies.

Acknowledgements

Appendix A. Supplementary data

Supplementary data to this article can be found online at https://doi.org/10.1016/j.quascirev.2018.09.034.

References

Alloway, B.V., Moreno, P.I., Pearce, N., De Pol-Holz, R., Henríquez, W., Pesce, O., Sagredo, E., Villarosa, G., Outes, V., 2017a. Stratigraphy, age and correlation of Lepué tephra: a widespread c. 11,000 cal. a BP marker horizon sourced from the Chaitén Sector of southern Chile. J. Quat. Sci. 32, 795–829.

Alloway, B.V., Pearce, N.J.G., Moreno, P.I., Villarosa, G., Jara, I., De Pol-Holz, R., Outes, V., 2017b. An 18,000 year-long eruptive record from Volcán Chaitén, northwestern Patagonia: paleoenvironmental and hazard-assessment implications. Quat. Sci. Rev. 168, 151–181.

Andersen, N.L., Singer, B.S., Jicha, B.R., Beard, B.L., Johnson, C.M., Licciardi, J.M., 2017. Pleistocene to Holocene growth of a large upper crustal rhyolitic magma reservoir beneath the active Laguna del Maule Volcanic Field, Central Chile. J. Petrol. 58, 85–114.

Bachmann, O., Bergantz, G.W., 2006. Percolation in upper crustal silicic crystal mushes as a mechanism for upward heat advection and rejuvenation of near solidus magma bodies. J. Volcanol. Geoth. Res. 149, 85–102.

Bacon, C.R., Druitt, T.H., 1988. Compositional evolution of the zoned calcalkaline magma chamber of Mount Mazama, Crater Lake, Oregon. Contrib. Mineral. Petrol. 98, 224–256.

Bonadonna, C., Costa, A., 2012. Estimating the volume of tephra deposits: a new simple strategy. Geology 40, 415–418.

Cashman, K.V., Sparks, S.R.J., 2014. How volcanoes work: a 25 year perspective.

Geol. Soc. Am. Bull. 125, 664–690. https://doi.org/10.1130/B30720.1.

Cashman, K.V., Sparks, S.R.J., Blundy, J.D., 2017. Vertically extensive and magmatic systems: a unified view of igneous processes. Science 355. https://doi.org/10.1126/science.aag3055.

Cembrano, J., Schermer, E., Lavenu, A., Sanhueza, A., 2000. Contrasting nature of deformation along an intra-arc shear zone, the Liquiñe–Ofqui fault zone, southern Chilean Andes. Tectonophysics 319, 129–149.

de Silva, S., 2001. Magmas in collision: rethinking chemical zonation in silicic magmas: comment and Reply COMMENT. Geology 29, 1063-1063.

Douglass, D.C., Singer, B.S., Kaplan, M.R., Ackert, R.P., Mickelson, D.M., Caffee, M.W., 2005. Evidence of early Holocene glacial advances in southern South America from cosmogenic surface-exposure dating. Geology 33, 237–240.

Eichelberger, J.C., Chertkoff, D.G., Dreher, S.T., Nye, C.J., 2000. Magmas in collision: rethinking chemical zonation in silicic magmas. Geology 28, 603–606.

Eichelberger, J.C., Chertkoff, D.G., Dreher, S.T., Nye, C.J., 2001. Reply. *Geology* 29, 1063–1064.

Fierstein, J., Nathenson, M., 1992. Another look at the calculation of fallout tephra volumes. Bull. Volcanol. 54, 156–167.

Firth, C., Handley, H., Turner, S., Cronin, S.J., Smith, I., 2016. Variable conditions of magma storage and differentiation with links to eruption style at Ambrym Volcano, Vanuatu. J. Petrol. 57, 1049–1072.

Fontijn, K., Lachowycz, S.M., Rawson, H., Pyle, D.M., Mather, T.A., Naranjo, J.A., Moreno-Roa, H., 2014. Late Quaternary tephrostratigraphy of southern Chile and Argentina. Quat. Sci. Rev. 89, 70–84.

Fontijn, K., Rawson, H., Van Daele, M., Moernaut, J., Abarzúa, A.M., Heirman, K., Bertrand, S., Pyle, D.M., Matherm, T.A., De Batist, M., Naranjo, J.-A., Moreno, H., 2016. Synchronisation of sedimentary records using tephra: a postglacial tephrochronological model for the Chilean Lake District. Quat. Sci. Rev. 137, 234–254.

Gutiérrez, F., Gioncada, A., González Ferran, O., Lahsen, A., Mazzuoli, R., 2005. The Hudson Volcano and surrounding monogenetic centres (Chilean Patagonia): an example of volcanism associated with ridge-Trench collision environment. J. Volcanol. Geoth. Res. 145, 207–233.

Henríquez, W.I., Moreno, P.I., Alloway, B.V., Villarosa, G., 2015. Vegetation and climate change, fire-regime shifts and Volcanic disturbance in Chiloé Continental (43°S) during the last 10,000 years. Quat. Sci. Rev. 123, 158–167.

Herman, F., Brandon, M., 2015. Mid-latitude glacial erosion hotspot related to equatorial shifts in southern Westerlies. Geology 43, 987–990.

Hernando, I.R., Petrinovic, A.A., Llambías, E.J., D'Elia, L., González, P.D., Aragón, E., 2016. The role of magma mixing and mafic recharge in the evolution of a back-arc Quaternary caldera: the case of Payún Matrú, western Argentina. J. Volcanol. Geoth. Res. 311, 150–169.

Hildreth, W., Drake, B., 1992. Volcán Quizapu, chilean Andes. Bull. Volcanol. 54, 93–125.

Holland, T., Blundy, J., 1994. Non-ideal interactions in calcic amphiboles and their bearing on amphibole-plagioclase thermometry. Contrib. Mineral. Petrol. 116, 433–447.

Jara, I.A., Moreno, P.I., 2012. Temperate rainforest response to climate change and disturbance agents in northwestern Patagonia (41°S) over the last 2600 years. QR (Quat. Res.) (N. Y.) 77, 235–244.

Kent, A.J.R., Darr, C., Koleszar, A.M., Salisbury, M.J., Cooper, K.M., 2010. Preferential eruption of andesitic magmas through recharge filtering. Nat. Geosci. 3, 631–636.

Kilian, R., Lamy, F., 2012. A review of Glacial and Holocene paleoclimate records from southernmost Patagonia (49–55°S). Quat. Sci. Rev. 53, 1–23.

Kratzmann, D.J., Carey, S., Scasso, R., Naranjo, J.-A., 2009. Compositional variations and magma mixing in the 1991 eruptions of Hudson Volcano, Chile. Bull. Volcanol. 71, 419–439.

Lange, R.A., Frey, H.M., Hector, J., 2009. A thermodynamic model for the plagioclase-liquid hygrometer/thermometer. Am. Mineral. 94, 494–506.

Le Maitre, R.W., 1984. A proposal by the IUGS Sub-Commission on the systematics of igneous rocks for a chemical classification of volcanic rocks based on total alkali silica (TAS) diagram. Aust. J. Earth Sci. 31, 243–255.

López-Escobar, L., Kilian, R., Kempton, P., Tagiri, M., 1993. Petrology and geochemistry of Quaternary rocks from the southern volcanic zone of the Andes between 41°30' and 46°00'S, Chile. Rev. Geol. Chile 20, 33–55. https://doi.org/10.5027/andgeoV22n2-a06.

Loucks, R.R., 1996. A precise olivine-augite Mg-Fe-exchange geothermometer. Contrib. Mineral. Petrol. 125, 140–150.

Moreno, P.I., Leon, A.L., 2003. Abrupt vegetation changes during the last glacial to Holocene transition in mid-latitude South America. J. Quat. Sci. 18, 787–800.

Moreno, P.I., Alloway, B.V., Henríquez, W.I., Villarosa, G., Outes, V., De Pol-Holz, R., Pearce, N.J.G., 2015. A past millennium maximum in postglacial activity from Volcán Chaitén, southern Chile. Geology 43, 47–50.

Moreno, P.I., Vilanova, I., Villa-Martínez, R., Dunbar, R.B., Mucciarone, D.A., Kaplan, M.R., Garreaud, R.D., Rojas, M., Moy, C.M., De Pol-Holz, R., Lambert, F., 2018. Onset and evolution of southern annular mode-like changes at centennial timescale. Sci. Rep. 8, 3458. https://doi.org/10.1038/s41598-018-21836-6.

International stratigraphic guide - an abridged edition. In: Murphy, M.A., Salvador, A. (Eds.), Episodes 22, 255–271.

Nakamura, N., 1974. Determination of REE, Ba, Fe, Mg, Na and K in carbonaceous and ordinary chondrites. Geochem. Cosmochim. Acta 38, 757–775.

Naranjo, J.A., Stern, C.R., 2004. Holocene tephrochronology of the southernmost part (42°30'-45°S) of the andean southern volcanic zone. Rev. Geol. Chile 31, 225–240.

Naranjo, J.A., Singer, B.S., Jicha, B.R., Moreno, H., Lara, L.E., 2017. Holocene tephra succession of Puyehue-Cordón Caulle and Antillanca/Casablanca volcanic complexes, southern Andes (40-41ºS). J. Volcanol. Geoth. Res. https://doi.org/10.1016/j.jvolgeores.2016.11.017.

Parfitt, E.A., Wilson, L., 2008. The role of volatiles. Fundamentals of Physical Volcanology 64–76.

Pearce, N.J.G., 2014. Towards a protocol for the analysis of rhyolitic glass shards in tephra deposits by laser ablation ICP-MS. J. Quat. Sci. 29, 627–640. https://doi.org/10.1002/jqs.2727. ISSN 0267-8179.

Pesce, O.H., Moreno, P.I., 2014. Vegetation, fire and climate change in central-east isla grande de Chiloé (43°S) since the last glacial maximum, northwestern Patagonia. Quat. Sci. Rev. 90, 143–157.

Putirka, K.D., 2008. Thermometers and barometers for volcanic systems. Rev. Mineral. Geochem. 69, 61–120.

Putirka, K.D., Mikaelian, H., Ryerson, F., Shaw, H., 2003. New clinopyroxene-liquid thermobarometers for mafic, evolved, and volatile-bearing lava compositions, with applications to lavas from Tibet and the Snake River Plain, Idaho. Am. Mineral. 88, 1542–1554.

Ridolfi, F., Renzulli, A., Puerini, M., 2010. Stability and chemical equilibrium of amphibole in calc-alkaline magmas: an overview, new thermobarometric formulations and application to subduction-related volcanoes. Contrib. Mineral. Petrol. 160, 45–66.

Rojas, M., Moreno, P., Kageyama, M., Crucifix, M., Hewitt, C., Abe-Ouchi, A., Hope, P., 2009. The Southern Westerlies during the last glacial maximum in PMIP2 simulations. Clim. Dynam. 32, 525–548.

Rojas, M., Moreno, P.I., 2011. Atmospheric circulation changes and neoglacial conditions in the Southern Hemisphere mid-latitudes: insights from PMIP2 simulations at 6 kyr. Clim. Dynam. 37, 357–375.

Ruprecht, P., Bergantz, G.W., Cooper, K.M., Hildreth, W., 2012. The crustal magma storage system of Volcán Quizapu, Chile, and the effects of magma mixing on magma diversity. J. Petrol. 53, 801–840.

Shane, P., Maas, R., Lindsay, J., 2017. History of Red Crater volcano, Tongariro Volcanic Centre (New Zealand): abrupt shift in magmatism following recharge and contrasting evolution between neighbouring volcanoes. J. Volcanol. Geoth. Res. 340, 1–15.

Singer, B.S., Jicha, B.R., Harper, M.A., Naranjo, J.A., Lara, L.E., Moreno-Roa, H., 2008. Eruptive history, geochronology, and magmatic evolution of the Puyehue–Cordón Caulle volcanic complex, Chile. Bull. Geol. Soc. Am. 120, 599–618.

Singer, B.S., Andersen, N.L., Le Mével, H., Feigl, K.L., DeMets, C., Tikoff, B., Thurber, C.H., Jicha, B.R., Cardona, C., Córdova, L., Gil, F., Unsworth, M.J., Williams-Jones, G., Miller, C., Fierstein, J., Hildreth, W., Vazquez, J., 2014. Dynamics of a large, restless, rhyolite magma system at Laguna del Maule, southern Andes, Chile. GSA Today (Geol. Soc. Am.) 24 (12), 4–10.

Singer, B.S., Costa, F., Herrin, J.S., Hildreth, W., Fierstein, J., 2016. The timing of compositionally-zoned magma reservoirs and mafic 'priming' weeks before the 1912 Novarupta-Katmai rhyolitic eruption. Earth Planet Sci. Lett. 451, 125–137.

Smith, R.L., 1979. Ash-flow magmatism. GSA (Geol. Soc. Am.) Spec. Pap. (Reg. Stud.) 180, 5–28.

Sparks, S.R.J., Cashman, K.V., 2017. Dynamic magma systems: implications for forecasting volcanic activity. Elements 13, 35–40. https://doi.org/10.2113/gselements.13.1.35.

Stern, C.R., 2004. Active Andean volcanism: its geologic and tectonic setting. Rev. Geol. Chile 31, 161–206.

Stern, C.R., Moreno, H., Lopez-Escobar, L., Clavero, J.E., Lara, L.E., Naranjo, J.A., Parada, M.A., Skewes, M.A., 2007. Chilean volcanoes. In: Moreno, T., Gibbons, W. (Eds.), The Geology of Chile. Geological Society of London, London, UK, pp. 147–178.

Stern, C.R., de Porras, M.E., Maldonaldo, A., 2015. Tephrochronology of the upper Rio Cisnes valley (44°S), southern Chile. Andean Geol. 42, 173–189.

Sun, S.S., McDonough, W.S., 1989. Chemical and isotopic systematics of oceanic basalts: implications for mantle composition and processes. Geological Society, London, Special Publications 42, 313–345.

Tait, S., Jaupart, C., Vergniolle, S., 1989. Pressure, gas content and eruption periodicity of a shallow, crystallising magma chamber. Earth Planet Sci. Lett. 92, 107–123.

Völker, D., Kutterolf, S., Wehrmann, H., 2011. Comparative mass balance of volcanic edifices at the southern volcanic zone of the Andes between 33°S and 46°S. J. Volcanol. Geoth. Res. 205, 114–129.

Weller, D.J., Miranda, C.G., Moreno, P.I., Villa-Martinez, R., Stern, C.R., 2014. The large late glacial Ho eruption of the Hudson Volcano, southern Chile. Bull. Volcanol. 76, 831–849.

Weller, D.J., Miranda, C.G., Moreno, P.I., Villa-Martinez, R., Stern, C.R., 2015. Tephrochronology of the southernmost andean southern volcanic zone, Chile. Bull. Volcanol. 77, 107. https://doi.org/10.1007/s00445-015-0991-2.

Weller, D.J., de Porras, M.E., Maldonaldo, A., Mendez, C., Stern, C.R., 2017. Holocene tephrochrononology of the lower Rio Cisnes valley, southern Chile. Andean Geol. 44, 229–248.

Wolff, J.A., Wörner, G., Blake, S., 1990. Gradients in physical parameters in zoned felsic magma bodies: implications for evolution and eruptive withdrawal. J. Volcanol. Geoth. Res. 43, 37–55.